Electronic Supplementary Information for:

Calcium-43 Chemical Shift and Electric Field Gradient Tensor Interplay: A Sensitive Probe of Structure, Polymorphism, and Hydration

Cory M. Widdifield,[ab]* Igor Moudrakovski,[ac#] and David L. Bryce[a]*

* Corresponding authors. E-mails: cory.widdifield@ens-lyon.fr; dbryce@uottawa.ca

[a] Department of Chemistry and Centre for Catalysis Research and Innovation, University of Ottawa, 10 Marie Curie Pvt., Ottawa, Ontario, Canada. Tel.: +1 613 562 5800 ext. 2018; Fax: +1 613 562 5170.

[b] Université de Lyon, Institut des Sciences Analytiques (CNRS, ENS-Lyon, UCB Lyon 1), Centre de RMN à Très Hauts Champs, 5 rue de la Doua, 69100, Villeurbanne, France. Tel.: +33 4 26 23 38 88; Fax: +33 4 78 89 67 61.

[c] Steacie Institute for Molecular Sciences, NRC, 100 Sussex Drive, Ottawa, K1A 0R6

[#] Current address: Max-Planck-Institute for Solid State Research, Heisenbergstraße 1, 70569 Stuttgart, Germany

Table of Contents

Additional Experimental.

Synthesis of (±)-calcium tartrate tetrahydrate. Crystallization was induced using a silica-based gel. To prepare the silica gel, approximately 50 mL of 0.5 M DL-tartaric acid was titrated with a solution of 0.5 M sodium metasilicate to a pH of 4. Subsequently, about 50 mL of the solution was placed into several large test tubes and allowed to set for a period of 48 hours. Once the gel had set, 15 mL of 0.5 M $CaCl_2$ was carefully added to each test tube. The test tubes were then stoppered and placed into a darkened water bath which was temperature regulated at 40 °C, and the reaction was allowed to progress for approximately five weeks. It is noted that after the addition of the $CaCl_2$ solution, approximately two weeks were required for the gel to re-set. After the five week incubation period, the resulting crystals were extracted from the gel using methanol. Specifically, the gel was placed onto a petri dish and methanol was added until the gel phase dissolved. The liquid phase was then removed. The product crystals were then placed into a Buchner funnel, rinsed thoroughly with methanol, and dried under suction.

Solid-State ^{13}C NMR. Data were primarily acquired at the University of Ottawa using a wide bore Bruker AVANCE III spectrometer operating at B_0 = 9.4 T ($\nu_0(^{13}C)$ = 100.62 MHz) and used a 4 mm HXY probe. The data for calcium acetate monohydrate were recorded at the National Research Council Canada (Montreal road campus) using a wide bore Bruker AVANCE spectrometer operating at 4.7 T ($\nu_0(^{13}C)$ = 50.41 MHz) and used a 7 mm HX probe. All ^{13}C solid-state NMR spectra were referenced using solid adamantane as an external secondary reference, and is such that the most deshielded ^{13}C NMR peak of adamantane is set to 38.52 ppm, as specified by Hayashi and Hayamizu.[1] Pulse calibrations were also carried out using adamantane. For further details, see Table S2.

Powder X-ray Diffraction. Measurements were carried out at the University of Ottawa with a Rigaku Ultima IV diffractometer using a Cu-Kα X-ray source (λ = 1.540598 Å). Typical 2θ scan ranges were between 5° and 80°. All measurements were carried out at ambient temperature and atmosphere. Simulations of powder X-ray diffractograms were generated using Diamond (ver. 3.2i, Crystal Impact GbR, Bonn, Germany).

SIMPSON simulation details. Numerical line shape simulations used version 4 of SIMPSON.[2] Simulations generally used the following parameters: γ angles = 50 – 70; powder averaging via the *zcw28656* file; start and detect operators were I_{1x} and I_{1p}, respectively; and the '*gcompute*' method was selected. After generating the time-domain points, they were Fourier-transformed and about 8 – 80 Hz of exponential line broadening was used.

Table S1. Detailed ^{43}Ca SSNMR experimental acquisition parameters[a]

compound	B_0 / T	window / kHz	ν_{MAS} / kHz[b]	points[c]	$\pi/2$ / μs[d]	scans	recycle delay / s	$\nu_{\mathrm{rf}}\{^1H\}$ / kHz	details
$Ca(OH)_2$	9.4	20.0	0	1024	7.5[e]	273600	0.7	33.3	CP from ^{1}H; 7 mm HX static probe; TPPM decoupling[3] during acquisition; 30 ms contact time; displayed in Figure 2; CP rf fields: ^{1}H = ca. 20 kHz; ^{43}Ca = ca. 7 kHz
	9.4	20.0	0	1024	7.5[e]	30000	0.7	33.3	Conditions used to generate CP build-up curve; all else is the same as directly above, except the use of a variable contact time; displayed in Figure 3
	11.75	40.0	0	3596	2.63	63228	4.0	0	Bloch decay; 10 mm X static probe; referenced to saturated $CaCl_2$(*aq*); displayed in Figure S3
	21.1	20.0	5.00	1024	2.0	6830	10.0	0	Bloch decay; 7 mm X MAS probe; displayed in Figure S1
	21.1	20.0	0	512	9.0[e]	28200	2.0	19.2	CP from ^{1}H; 7 mm HX static probe; SPINAL64 decoupling[4] during acquisition; 20 ms contact time; displayed in Figure 2; optimized CP rf fields: ^{1}H = 24.8 kHz; ^{43}Ca = 6.4 kHz
	21.1	20.0	0	512	9.0[e]	10800	2.0	0	same as directly above, except no ^{1}H decoupling during acquisition; displayed in Figure S5
	21.1	20.0	0	512	9.0[e]	512	2.0	19.2	Conditions used to generate Figure S4; CP from ^{1}H; 7 mm HX static probe; SPINAL64 decoupling during acquisition; 20 ms contact time; variable contact power on the ^{43}Ca channel, while the ^{1}H rf field was maintained at 24.8 kHz
α-$Ca(CHO_2)_2$	9.4	20.0	5.00	1912	5.5	21144	10.0	0	Bloch decay; 7 mm HX MAS probe; displayed in Figure S8
	21.1	20.0	5.00	1024	2.0	4096	5.0	0	Bloch decay; 7 mm X MAS probe; displayed in Figure S8
	21.1	20.0	0	512	1.6	15952	10.0	19.2	Bloch decay; 7 mm HX static probe; SPINAL64 decoupling during acquisition; displayed in Figure 4, T = 295(1) K
$CaCl_2 \cdot 2H_2O$	11.75	40.0	0	600	2.4	47787	5.0	0	Bloch decay; 10 mm X static probe; referenced to saturated $CaCl_2$(*aq*); displayed in Figure S9
	21.1	20.0	4.50	2048	1.8	7920	10.0	0	Bloch decay; 7 mm X MAS probe; displayed in Figure 5
	21.1	20.0	0	512	1.6	7220	10.0	19.2	Bloch decay; 7 mm HX static probe; SPINAL64 decoupling during acquisition; displayed in Figure 5
(±)-$Ca(C_4H_4O_6) \cdot 4H_2O$	21.1	20.0	5.00	1024	1.8	4896	7.0	0	Bloch decay; 7 mm X MAS probe; displayed in Figure 6

compound	$\mathbf{B}_0$ / T	window / kHz	ν_{MAS} / kHz[b]	points[c]	$\pi/2$ / μs[d]	scans	recycle delay / s	$\nu_{\mathrm{rf}}\{^1\mathrm{H}\}$ / kHz	details
	21.1	20.0	0	512	2.0	24000	10.0	19.2	Bloch decay; 7 mm HX static probe; continuous wave (cw) decoupling during acquisition; displayed in Figure 6
$Ca(C_2H_3O_2)_2 \cdot H_2O$	9.4	5.0	5.00	1024	45.0[h]	768	9.0	0	multiple-Gaussian-RAPT;[5] 7 mm HX MAS probe; displayed in Figure S13
	9.4	10.0	0	1024	45.0	4096	9.0	28	Hahn echo; 7 mm HX MAS probe; echo delay = 149.5 μs; cw decoupling during acquisition; displayed in Figure S13
	21.1	39.682	0	1024	10.0	256	30.0	25	Hahn echo; 7 mm HX static probe; echo delay = 200 μs; cw decoupling during acquisition; displayed in Figure 7
	21.1	20.0	5.00	2048	2.25	64	5.0	0	Bloch decay; 7 mm X MAS probe; displayed in Figure 7
$Ca(C_5H_7O_3)_2 \cdot 2H_2O$	21.1	20.0	4.50	2048	1.8	8495	10.0	0	Bloch decay; 7 mm X MAS probe; displayed in Figure 8
$CaSO_4 \cdot 2H_2O$	9.4	5.0	5.00	1024	50.0[f]	32	250	0	DFS/echo; 7 mm HX MAS probe; displayed in Figure S18
	9.4	10.0	0	1024	50.0	336	180	31	Hahn echo; 7 mm HX MAS probe; echo delay = 150 μs; cw decoupling during acquisition; displayed in Figure S18
	21.1	20.0	5.00	2048	2.25	32	200	0	Bloch decay; 7 mm X MAS probe; displayed in Figure 9
	21.1	29.762	0	1024	2.3	112	200	25	Bloch decay; 7 mm HX static probe; cw decoupling during acquisition; displayed in Figure 9
$CaCrO_4$	9.4	10.0	4.00	1024	2.3	65536	2.0	0	Bloch decay; 7 mm HX MAS probe; displayed in Figure S20
	21.1	100.0	4.00	3960	2.25	22722	3.0	0	Bloch decay; 7 mm X MAS probe; displayed in Figure 10
	21.1	50.0	0	2048	3.5	37485	0.5	0	Bloch decay; 10 mm X static probe; referenced to 1 M $CaCl_2$(*aq*); displayed in Figure 10
$CaTiO_3$	11.75	25.0	0	512	4.0	34816	5.0	0	Hahn echo; 10 mm HX static probe; echo delay = 1 ms; referenced to 1 M $CaCl_2$(*aq*); displayed in Figure S22
	21.1	20.0	5.00	1024	2.25	13133	5.0	0	Bloch decay; 7 mm X MAS probe; displayed in Figure 11
	21.1	50.0	0	1912	3.5	29071	5.0	0	Bloch decay; 10 mm X static probe; referenced to 1 M $CaCl_2$(*aq*); displayed in Figure 11
$Ca(NO_3)_2$	9.4	5.0	5.00	1024	100[g]	64	15.0	0	DFS/echo; 7 mm HX MAS probe; displayed in Figure S23
	9.4	10.0	0	1024	50	192	15.0	0	Hahn echo; echo delay = 100 μs; 7 mm HX MAS probe; displayed in Figure S23

compound	$\mathbf{B}_0$ / T	window / kHz	ν_{MAS} / kHz[b]	points[c]	$\pi/2$ / μs[d]	scans	recycle delay / s	$\nu_{\mathrm{rf}}\{^1\mathrm{H}\}$ / kHz	details
	21.1	20.0	5.00	8192	2.25	64	7.0	0	Bloch decay; 7 mm X MAS probe; displayed in Figure 12
	21.1	20.0	0	8192	100	640	10.0	0	Bloch decay; 7 mm X static probe; displayed in Figure 12
CaH_2	9.4	8.012	2.50	2048	5.0	24576	10.0	0	Bloch decay; 14 mm X MAS probe; displayed in Figure S25
	11.75	10.0	6.00	1200	2.5	8192	60.0	35	Bloch decay; 6 mm T3 MAS probe; SPINAL64 decoupling during acquisition; referenced to 1 M $CaCl_2$(*aq*); displayed in Figure S25
	21.1	20.0	5.00	4096	2.25	3072	40.0	0	Bloch decay; 7 mm X MAS probe; displayed in Figure 13
	21.1	29.76	0	1024	2.0	5216	40.0	25	Bloch decay; 7 mm HX static probe; cw decoupling during acquisition; displayed in Figure 13
$CaCO_3$, coral	11.75	5.0	5.00	2048	2.25	65440	2.0	0	Bloch decay; 6 mm T3 MAS probe; displayed in Figure S27
	21.1	50.0	0	1024	3.5	20000	1.5	0	Bloch decay; 10 mm X static probe; referenced to 1 M $CaCl_2$(*aq*); displayed in Figure 14
$CaCO_3$, clam pearl	21.1	100.0	3.00	3960	2.25[i]	16384	2.1	0	Bloch decay; 7 mm X MAS probe; displayed in Figure S27
	21.1	50.0	0	1024	3.5	12000	2.0	0	Bloch decay; 10 mm X static probe; referenced to 1 M $CaCl_2$(*aq*); displayed in Figure 14

[a] Unless denoted otherwise, experiments were conducted at room temperature, and were referenced to 2 M $CaCl_2$(*aq*).

[b] A value of 0 in this column denotes that the experiment took place under static (i.e., non-spinning) conditions.

[c] Complex time-domain data points.

[d] Corresponds to central-transition selective pulse length, unless otherwise denoted. Hence, to calculate the non-selective $\pi/2$ pulse length, multiply the value in this cell by 4.

[e] Corresponds to ^{1}H saturation pulse length.

[f] Central-transition (CT) was enhanced by a DFS pulse (2 ms in duration and sweeping from ±220 kHz to ±40 kHz) prior to the CT-selective pulse.

[g] CT enhanced by DFS pulse (2ms; ±250 kHz to ±35 kHz) prior to CT-selective pulse.

[h] While this pulse corresponds to a CT selective pulse, multiple-Gaussian-shaped RAPT preparation pulses (25 μs length for one saturating pulse (X), basic $X\overline{X}$ block, 16 blocks (multi-RAPT time was ca. 800 μs), $\nu_{\mathrm{off}} = \pm 90$ kHz) were applied prior to this pulse.

[i] Non-selective pulse.

Table S2. Detailed ^{13}C SSNMR experimental acquisition parameters[a]

compound	window / kHz	ν_{MAS} / kHz	points	$\pi/2$ / μs	scans	contact time / ms	recycle delay / s	$\nu_{rf}\{^1H\}$ / kHz	details
α-$Ca(CHO_2)_2$	33.333	5.0	3330	3.5	4208	2.5	20.0	56.7	Displayed in Figure S7
(±)-$Ca(C_4H_4O_6)\cdot 4H_2O$	33.333	5.0	3330	3.5	44400	2.5	2.0	56.7	Displayed in Figure S10
$Ca(C_2H_3O_2)_2\cdot H_2O$	12.019	5.0	3072	4.0	256	2.0	4.0	62.5	7 mm HX probe; displayed in Figure S14
$Ca(C_5H_7O_3)_2\cdot 2H_2O$	33.333	5.5	3330	3.5	13840	2.5	5.0	56.7	Displayed in Figure S16

[a] Unless specified otherwise, all experiments were performed at room temperature with a 4 mm HXY probe, used CP from the abundant ^1H nuclei, and employed heteronuclear decoupling during signal acquisition with the SPINAL64 sequence.[4] All ^{13}C NMR spectra were referenced using solid adamantane ($\delta_{iso}(^{13}C, \underline{C}H_2) = 38.52$ ppm).[1]

Table S3. GIPAW DFT quantum chemical H atom geometry optimizations – pseudopotential files used, energies and structure references[a]

compound	pseudopotential files used	energy / eV	structure reference(s) and additional details
β-$Ca(CHO_2)_2$	H_00PBE.usp; O_00PBE.usp; C_00PBE.usp; Ca_00PBE.usp	−12380.645799	Matsui *et al.*[6] 4 × 4 × 3 *k*-point grid (24 points)
$CaCl_2\cdot 2H_2O$	H_00PBE.usp; O_00PBE.usp; Cl_00PBE.usp; Ca_00PBE.usp	−11054.255714	Leclaire & Borel.[7] 4 × 3 × 2 *k*-point grid (12 points)
$Ca(C_4H_4O_6)\cdot 3H_2O$	H_00PBE.usp; C_00PBE.usp; O_00PBE.usp; Ca_00PBE.usp	−22876.647390	de Vries & Kroon.[8] 3 × 2 × 3 *k*-point grid (9 points)
(+)-$Ca(C_4H_4O_6)\cdot 4H_2O$	H_00PBE.usp; C_00PBE.usp; O_00PBE.usp; Ca_00PBE.usp	−24752.791591	Hawthorne *et al.*[9] 3 × 2 × 3 *k*-point grid (9 points)
(±)-$Ca(C_4H_4O_6)\cdot 4H_2O$	H_00PBE.usp; C_00PBE.usp; O_00PBE.usp; Ca_00PBE.usp	−12377.071595	Le Bail *et al.*[10] 4 × 3 × 3 *k*-point grid (18 points)
$Ca(C_2H_3O_2)_2\cdot H_2O$ (1984)	H_00PBE.usp; C_00PBE.usp; O_00PBE.usp; Ca_00PBE.usp	−15759.116545	Klop *et al.*[11] 4 × 3 × 2 *k*-point grid (12 points); first reported polymorph
$Ca(C_2H_3O_2)_2\cdot H_2O$ (1987)	H_00PBE.usp; C_00PBE.usp; O_00PBE.usp; Ca_00PBE.usp	−15759.250163	van der Sluis *et al.*[12] 4 × 3 × 2 *k*-point grid (12 points); second reported polymorph
$CaSO_4\cdot 2H_2O$	H_00PBE.usp; O_00PBE.usp; S_00PBE.usp; Ca_00PBE.usp	−15882.199930	Comodi *et al.*[13] 4 × 2 × 5 *k*-point grid (20 points)
$Ca(NO_3)_2$	N_00PBE.usp; O_00PBE.usp; Ca_00PBE.usp	−16647.497430	Vegard & Bilberg.[14] 3 × 3 × 3 *k*-point grid (14 points)

[a] All GIPAW DFT geometry optimizations used the PBE XC functional,[15,16] as described in the main text. All calculations used the 'precise' setting for the fast Fourier transformation grid and $E_{cut} = 800$ eV, where E_{cut} = plane wave basis set energy cut-off. Optimized structure parameters can be found in Table S6. In the case of $Ca(NO_3)_2$, due to the age of the diffraction data (1931 publication), refinement was carried out for the N and O atomic positions. Basis set convergence was tested and ensured for all systems.

Table S4. GIPAW DFT magnetic shielding and EFG tensor calculations – pseudopotential files used, energies and structure references[a]

compound	pseudopotential files used[b]	energy / eV	structure reference(s) and additional details[c]
$Ca(OH)_2$	H_00PBE.usp; O_00PBE.usp	−1913.572316	Desgranges *et al.*[17] E_{cut} = 1200 eV; 8 × 8 × 6 *k*-point grid (45 points)
α-$Ca(CHO_2)_2$	H_00PBE.usp; O_00PBE.usp; C_00PBE.usp	−24775.852840	Burger *et al.*[18] E_{cut} = 1000 eV; 2 × 2 × 4 *k*-point grid (2 points)
β-$Ca(CHO_2)_2$	H_00PBE.usp; C_00PBE.usp; O_00PBE.usp	−12387.417270	Matsui *et al.*[6] E_{cut} = 1000 eV; 4 × 4 × 3 *k*-point grid (6 points)
$CaCl_2{\cdot}2H_2O$	H_00PBE.usp; O_00PBE.usp; Cl_00PBE.usp	−11060.792100	Leclaire & Borel.[7] E_{cut} = 800 eV; 4 × 3 × 2 *k*-point grid (4 points)
$Ca(C_4H_4O_6){\cdot}3H_2O$	H_00PBE.usp; C_00.otfg; O_00PBE.usp	−22925.544620	de Vries & Kroon.[8] E_{cut} = 1000 eV; 3 × 2 × 3 *k*-point grid (5 points)
(+)-$Ca(C_4H_4O_6){\cdot}4H_2O$	H_00PBE.usp; C_00.otfg; O_00PBE.usp	−24801.756070	Hawthorne *et al.*[9] E_{cut} = 1000 eV; 3 × 2 × 3 *k*-point grid (4 points)
(±)-$Ca(C_4H_4O_6){\cdot}4H_2O$	H_00PBE.usp; C_00PBE.usp; O_00PBE.usp	−12380.666253	Le Bail *et al.*[10] E_{cut} = 1000 eV; 4 × 3 × 3 *k*-point grid (18 points)
$Ca(C_2H_3O_2)_2{\cdot}H_2O$ (1984)	H_00PBE.usp; C_00.otfg; O_00PBE.usp	−15807.731070	Klop *et al.*[11] E_{cut} = 1000 eV; 4 × 3 × 2 *k*-point grid (12 points); first reported polymorph
$Ca(C_2H_3O_2)_2{\cdot}H_2O$ (1987)	H_00PBE.usp; C_00.otfg; O_00PBE.usp	−15807.859863	van der Sluis *et al.*[12] E_{cut} = 1000 eV; 4 × 3 × 2 *k*-point grid (12 points); second reported polymorph
$CaSO_4{\cdot}2H_2O$	H_00PBE.usp; O_00.otfg; S_00.otfg	−8006.500243	Comodi *et al.*[13] E_{cut} = 1000 eV; 5 × 5 × 5 *k*-point grid (39 points)
$CaCrO_4$	O_00PBE.usp; Cr_00.otfg	−20813.186909	Weber & Range.[19] E_{cut} = 1000 eV; 3 × 3 × 3 *k*-point grid (6 points)
$CaTiO_3$	O_00.otfg; Ti_00.otfg	−15709.186466	Ali & Yashima.[20] E_{cut} = 1000 eV; 5 × 5 × 3 *k*-point grid (18 points)
$Ca(NO_3)_2$	N_00PBE.usp; O_00PBE.usp	−16648.449486	Vegard & Bilberg.[14] E_{cut} = 1000 eV; 4 × 4 × 4 *k*-point grid (4 points); exactly as reported.
$Ca(NO_3)_2$	N_00PBE.usp; O_00PBE.usp	−16650.782485	Vegard & Bilberg.[14] E_{cut} = 1000 eV; 4 × 4 × 4 *k*-point grid (4 points); geometry optimized N and O atoms.
CaH_2	H_00PBE.usp	−4146.372463	Alonso *et al.*[21] E_{cut} = 1000 eV; 4 × 7 × 4 *k*-point grid (16 points)

[a] All GIPAW DFT computations of EFG and magnetic shielding tensor parameters used the PBE XC functional, as described in the main text. Full details of the computed parameters can be found in Table S5. All calculations used the 'precise' setting for the fast Fourier transformation grid.

[b] The updated string was used for the generation of the calcium pseudopotential in all calculations (i.e., Ca_01.otfg). In the format used by Materials Studio, it is "3|1.6|2|1.4|7.5|9.2|10.3|30U=-1.72:40U=-0.14:31U=-1.03U=+0.25:32U=+0U=+1[]".

[c] E_{cut} = plane wave basis set energy cut-off. Basis set convergence was tested and ensured for all systems.

Table S5. GIPAW DFT computed calcium EFG and magnetic shielding tensor parameters – additional information[a]

compound	site label	V_{11} / a.u.	V_{22} / a.u.	V_{33} / a.u.	C_Q(X) / MHz	η_Q	σ_{11} / ppm	σ_{22} / ppm	σ_{33} / ppm	Ω / ppm	κ	δ_{iso}[b] / ppm
$Ca(OH)_2$	—	−0.1093	−0.1093	0.2185	−2.283	0.000	1018.17	1056.61	1056.65	38.48	−0.998	71.93
α-$Ca(CHO_2)_2$	—	−0.0068	−0.1277	0.1345	−1.405	0.899	1096.63	1114.25	1126.26	29.63	−0.190	14.10
β-$Ca(CHO_2)_2$	—	−0.0901	−0.1836	0.2737	−2.859	0.342	1111.19	1129.67	1151.95	40.76	0.094	−1.55
$CaCl_2 \cdot 2H_2O$	—	0.1298	0.1894	−0.3192	3.335	0.187	1042.23	1051.19	1067.70	25.47	0.296	63.58
$Ca(C_4H_4O_6) \cdot 3H_2O$	—	0.0389	0.1217	−0.1660	1.734	0.499	1080.19	1099.73	1116.65	36.46	−0.072	25.51
(+)-$Ca(C_4H_4O_6) \cdot 4H_2O$	—	−0.0203	−0.0889	0.1092	−1.141	0.628	1106.70	1124.75	1136.66	29.96	−0.205	5.40
(±)-$Ca(C_4H_4O_6) \cdot 4H_2O$	—	0.0136	0.0808	−0.0943	0.985	0.713	1116.77	1121.03	1133.72	16.96	0.497	4.43
$Ca(C_2H_3O_2)_2 \cdot H_2O$ (1984)	1	−0.0582	−0.1254	0.1836	−1.918	0.366	1113.78	1146.02	1152.49	38.70	−0.666	−7.03
	2	−0.0595	−0.0699	0.1294	−1.352	0.080	1095.38	1110.88	1118.06	22.67	−0.367	17.71
$Ca(C_2H_3O_2)_2 \cdot H_2O$ (1987)	1	−0.0643	−0.0874	0.1517	−1.585	0.152	1111.31	1149.25	1154.86	43.55	−0.743	−7.90
	2	−0.0322	−0.1425	0.1748	−1.826	0.631	1093.67	1116.22	1125.06	31.38	−0.437	14.72
$CaSO_4 \cdot 2H_2O$	—	−0.0001	−0.1389	0.1390	−1.452	0.999	1119.51	1161.03	1177.15	57.64	−0.441	−19.79
$CaCrO_4$	—	−0.0644	−0.0644	0.1288	−1.346	0.000	1146.23	1232.05	1232.05	85.82	−1.000	−62.70
$CaTiO_3$	—	0.0299	0.1585	−0.1884	1.968	0.683	1076.22	1096.40	1145.84	69.62	0.420	19.35
$Ca(NO_3)_2$ (original)	—	0.1665	0.1665	−0.3331	3.480	0.000	1174.43	1174.43	1213.81	39.38	1.000	−49.30
$Ca(NO_3)_2$ (N,O opt)	—	0.1301	0.1301	−0.2602	2.718	0.000	1192.22	1192.22	1219.86	27.64	1.000	−61.00
CaH_2	—	0.0082	0.1007	−0.1089	1.138	0.849	971.69	981.41	1006.97	35.28	0.449	120.10

[a] $Q(^{43}Ca) = -4.44(6) \times 10^{-30}$ m^2 using the updated value in ref. 22. To convert $V_{33}(^{43}Ca)$ into frequency units, a conversion factor of −10.446534 MHz/a.u. was used where the unit EFG is $9.71736166 \times 10^{21}$ J C^{-1} m^{-2}.

[b] To map calculated magnetic shielding (σ) values into chemical shift (δ) values, the result of Moudrakovski *et al*. is used, as specified in ref. 23: δ_{iso} (ppm) = (1129.1 − σ_{iso} (ppm))/(1.1857).

Table S6. Atomic coordinates used for GIPAW DFT quantum chemical computations

atom	Wyckoff position	site symmetry	X[a]	Y[a]	Z[a]
$Ca(OH)_2$[b]					
Ca	1*a*	$\bar{3}m$	0.0000	0.0000	0.0000
O	2*d*	3*m*	0.3333	0.6666	−0.2337
H	2*d*	3*m*	0.3333	0.6666	−0.4224
α-$Ca(CHO_2)_2$[c]					
Ca	8*c*	1	−0.1345	−0.1073	−0.0277
O	8*c*	1	−0.0357	0.0473	−0.1906
O	8*c*	1	−0.2014	−0.0144	−0.3665
O	8*c*	1	−0.2001	−0.2014	0.2848
O	8*c*	1	−0.0236	−0.2981	0.2894
C	8*c*	1	−0.1130	0.0489	−0.3444
C	8*c*	1	−0.1260	−0.2659	0.3683
H	8*c*	1	−0.6013	−0.1071	−0.0369
H	8*c*	1	−0.6555	−0.7059	−0.0224
β-$Ca(CHO_2)_2$[d]					
Ca	4*a*	2	0.2169	0.2169	0.0000
O	8*b*	1	0.2766	0.0651	0.2353
O	8*b*	1	0.2813	0.3793	0.2851
C	8*b*	1	0.3039	0.2061	0.3170
H[e]	8*b*	1	0.3545	0.1703	0.4261
$CaCl_2\cdot 2H_2O$[f]					
Ca	4*c*	2	0.0000	0.2157	0.2500
Cl	8*d*	1	−0.2725	0.4509	0.1380
O	8*d*	1	0.2645	0.2107	0.1082
H[e]	8*d*	1	0.4133	0.2713	0.1136
H[e]	8*d*	1	0.2614	0.1496	0.0355
$Ca(C_4H_4O_6)\cdot 3H_2O$[g]					
Ca	4*e*	1	0.1867	0.0692	0.2141
C	4*e*	1	0.2747	0.8286	0.0231
C	4*e*	1	0.1955	0.7540	0.1339
C	4*e*	1	0.0918	0.6476	0.0756
C	4*e*	1	−0.0528	0.7098	0.0182
O	4*e*	1	0.2654	0.9515	0.0253
O	4*e*	1	0.3460	0.7640	−0.0595

atom	Wyckoff position	site symmetry	X^a	Y^a	Z^a
O	4*e*	1	0.1155	0.8426	0.2150
O	4*e*	1	0.0515	0.5574	0.1778
O	4*e*	1	−0.1712	0.6945	0.0803
O	4*e*	1	−0.0387	0.7761	−0.0877
O	4*e*	1	0.3954	0.9859	0.3387
O	4*e*	1	0.3649	0.2200	0.1316
O	4*e*	1	0.3131	0.4605	0.2718
H^e	4*e*	1	0.2843	0.7054	0.1956
H^e	4*e*	1	0.1492	0.5976	−0.0063
H^e	4*e*	1	0.0676	0.7946	0.2909
H^e	4*e*	1	0.1465	0.5147	0.2146
H^e	4*e*	1	0.4983	0.9859	0.3034
H^e	4*e*	1	0.3831	0.9020	0.3863
H^e	4*e*	1	0.3147	0.2554	0.0478
H^e	4*e*	1	0.4733	0.2104	0.1106
H^e	4*e*	1	0.3081	0.4800	0.3715
H^e	4*e*	1	0.3214	0.3659	0.2571
(+)-$Ca(C_4H_4O_6)\cdot 4H_2O^h$					
Ca	4*a*	1	0.3177	0.6772	0.1865
C	4*a*	1	0.6495	0.7027	0.1085
C	4*a*	1	0.6596	0.7273	0.2716
C	4*a*	1	0.7219	0.8584	0.2971
C	4*a*	1	0.7385	0.8928	0.4577
O	4*a*	1	0.5316	0.6730	0.0578
O	4*a*	1	0.7584	0.7154	0.0377
O	4*a*	1	0.5263	0.7157	0.3369
O	4*a*	1	0.6416	0.9545	0.2268
O	4*a*	1	0.7628	0.8086	0.5481
O	4*a*	1	0.7319	1.0103	0.4850
O	4*a*	1	0.8360	0.5901	0.7735
O	4*a*	1	0.4345	0.3304	0.6933
O	4*a*	1	0.5855	0.4270	0.9254
O	4*a*	1	0.4242	0.0635	0.9299
H^e	4*a*	1	0.8045	0.5534	0.8660
H^e	4*a*	1	0.9367	0.5703	0.7684

atom	Wyckoff position	site symmetry	X[a]	Y[a]	Z[a]
H[e]	4*a*	1	0.4904	0.3489	0.7819
H[e]	4*a*	1	0.4840	0.2704	0.6295
H[e]	4*a*	1	0.5507	0.5058	0.9707
H[e]	4*a*	1	0.6052	0.3669	1.0041
H[e]	4*a*	1	0.4712	−0.0137	0.8947
H[e]	4*a*	1	0.3403	0.0739	0.8704
H[e]	4*a*	1	0.7316	0.6569	0.3168
H[e]	4*a*	1	0.8279	0.8582	0.2513
H[e]	4*a*	1	0.5372	0.6664	0.4288
H[e]	4*a*	1	0.6862	0.9656	0.1258
(±)-$Ca(C_4H_4O_6)\cdot 4H_2O$[i]					
Ca	2*i*	1	0.6596	0.8099	0.7262
O	2*i*	1	0.3163	0.9767	1.0927
O	2*i*	1	1.1726	0.9733	1.3928
O	2*i*	1	0.9111	1.0269	1.1676
O	2*i*	1	0.6207	1.0217	1.3327
O	2*i*	1	0.9267	0.7075	1.3736
O	2*i*	1	0.2977	0.7032	1.0343
O	2*i*	1	0.3993	0.6866	0.4955
O	2*i*	1	0.8583	0.6536	0.6164
O	2*i*	1	0.3111	0.6239	0.7705
O	2*i*	1	0.8104	0.6476	0.8984
C	2*i*	1	0.9834	0.8492	1.3352
C	2*i*	1	0.3817	0.8494	1.1127
C	2*i*	1	0.8071	0.8711	1.2081
C	2*i*	1	0.5809	0.8668	1.2429
H[e]	2*i*	1	0.3207	0.5600	0.4553
H[e]	2*i*	1	0.2647	0.7291	0.4669
H[e]	2*i*	1	0.8879	0.6901	0.5322
H[e]	2*i*	1	1.0167	0.6612	0.6765
H[e]	2*i*	1	0.3097	0.6437	0.8657
H[e]	2*i*	1	0.2381	0.4969	0.7322
H[e]	2*i*	1	0.9834	0.6730	0.9411
H[e]	2*i*	1	0.7381	0.5266	0.9086
H[e]	2*i*	1	0.7602	0.7577	0.1277

atom	Wyckoff position	site symmetry	X[a]	Y[a]	Z[a]
H[e]	2*i*	1	0.5256	0.7520	0.2890
H[e]	2*i*	1	0.6838	1.0094	0.4292
H[e]	2*i*	1	0.8290	1.0227	0.0689
$Ca(C_2H_3O_2)_2 \cdot H_2O$ (1984)[j]					
Ca	2*i*	1	0.2263	0.0572	−0.0726
Ca	2*i*	1	0.4048	0.1731	0.2904
O	2*i*	1	0.0961	−0.1083	0.0054
O	2*i*	1	0.4093	−0.0438	0.0916
O	2*i*	1	0.4341	0.4095	0.3133
O	2*i*	1	0.3565	0.2425	0.1211
O	2*i*	1	0.2276	0.1786	−0.1851
O	2*i*	1	0.3780	0.1730	−0.3481
O	2*i*	1	−0.0519	−0.1330	−0.2637
O	2*i*	1	0.2666	−0.1511	−0.2532
O	2*i*	1	0.4658	0.3125	0.5130
O	2*i*	1	0.3790	0.0100	0.3697
C	2*i*	1	0.2511	−0.1316	0.0489
C	2*i*	1	0.2480	−0.2669	0.0480
C	2*i*	1	0.3767	0.3680	0.1989
C	2*i*	1	0.3300	0.4651	0.1485
C	2*i*	1	0.2459	0.2046	−0.2750
C	2*i*	1	0.1010	0.2880	−0.2930
C	2*i*	1	0.0875	−0.1999	−0.3007
C	2*i*	1	0.0450	−0.3454	−0.4001
H[e]	2*i*	1	0.4407	0.2678	0.5695
H[e]	2*i*	1	0.5020	0.4126	0.5704
H[e]	2*i*	1	0.4684	−0.0610	0.3526
H[e]	2*i*	1	0.3548	0.0446	0.4597
H[e]	2*i*	1	0.3818	0.7311	0.1023
H[e]	2*i*	1	0.4712	0.5220	0.1419
H[e]	2*i*	1	0.1316	0.3148	0.6299
H[e]	2*i*	1	−0.1102	0.6244	0.5551
H[e]	2*i*	1	0.2398	0.6541	−0.0514
H[e]	2*i*	1	0.2466	0.5412	0.2142
H[e]	2*i*	1	0.1044	0.3821	0.7963

atom	Wyckoff position	site symmetry	X[a]	Y[a]	Z[a]
H[e]	2*i*	1	0.0730	0.5896	0.6452
H[e]	2*i*	1	0.1117	0.7090	0.0864
$Ca(C_2H_3O_2)_2 \cdot H_2O$ (1987)[k]					
Ca	2*i*	1	0.2187	0.0573	0.4037
Ca	2*i*	1	0.5418	0.3341	0.4151
O	2*i*	1	0.6060	0.1839	0.6029
O	2*i*	1	0.5656	0.4128	0.5987
O	2*i*	1	0.2129	0.3036	0.4180
O	2*i*	1	0.8995	0.2930	0.3902
O	2*i*	1	0.5829	0.0746	0.3973
O	2*i*	1	0.9174	−0.0310	0.4035
O	2*i*	1	0.2041	0.1135	0.2138
O	2*i*	1	0.2040	0.3268	0.1156
O	2*i*	1	0.5169	0.3717	0.2233
O	2*i*	1	0.7768	0.4994	0.0896
C	2*i*	1	0.6034	0.2855	0.6524
C	2*i*	1	0.6413	0.2549	0.7745
C	2*i*	1	1.0275	0.3655	0.3874
C	2*i*	1	0.9641	0.5246	0.3456
C	2*i*	1	0.7498	0.0131	0.3515
C	2*i*	1	0.7467	−0.0081	0.2348
C	2*i*	1	0.1916	0.1993	0.1251
C	2*i*	1	0.1483	0.1519	0.0227
H[e]	2*i*	1	0.6021	0.4192	0.1666
H[e]	2*i*	1	0.4005	0.3562	0.1850
H[e]	2*i*	1	0.7722	0.5638	0.0154
H[e]	2*i*	1	0.9241	0.4434	0.1002
H[e]	2*i*	1	0.5095	0.7348	0.1818
H[e]	2*i*	1	0.2612	0.8556	0.1993
H[e]	2*i*	1	0.2927	0.6651	0.2015
H[e]	2*i*	1	0.2017	0.0342	0.0301
H[e]	2*i*	1	0.2173	0.2041	−0.0516
H[e]	2*i*	1	−0.0210	0.1856	0.0102
H[e]	2*i*	1	0.1452	0.4212	0.5951
H[e]	2*i*	1	−0.0982	0.4314	0.6649

atom	Wyckoff position	site symmetry	X[a]	Y[a]	Z[a]
H[e]	$2i$	1	0.1175	0.4522	0.7335
H[e]	$2i$	1	0.1783	1.1219	0.7699
H[e]	$2i$	1	0.4112	0.9755	0.7973
H[e]	$2i$	1	0.1591	0.9445	0.8169
$CaSO_4\cdot 2H_2O$[l]					
Ca	$4e$	2	0.0000	0.1705	0.2500
S	$4e$	2	0.0000	0.3273	0.7500
O	$8f$	1	0.0832	0.2722	0.5910
O	$8f$	1	0.2000	0.3819	0.9130
O	$8f$	1	−0.2082	0.0683	−0.0783
H[e]	$8f$	1	0.7467	0.0883	0.7414
H[e]	$8f$	1	0.7590	0.0046	0.9130
$CaCrO_4$[m]					
Ca	$4a$	$\bar{4}m2$	0.0000	0.7500	0.1250
Cr	$4b$	$\bar{4}m2$	0.0000	0.2500	0.3750
O	$16h$	m	0.0000	0.5694	0.7849
$CaTiO_3$[n]					
Ca	$4c$	m	−0.0078	0.0357	0.2500
Ti	$4b$	$\bar{1}$	0.0000	0.5000	0.0000
O	$4c$	m	0.0736	0.4828	0.2500
O	$8d$	1	0.7113	0.2893	0.0375
$Ca(NO_3)_2$[o] (original)					
Ca	$4a$	$\bar{3}$	0.0000	0.0000	0.0000
N	$8c$	3	0.3390	0.3390	0.3390
O	$24d$	1	0.2530	0.2930	0.4670
$Ca(NO_3)_2$ (N, O opt)					
Ca	$4a$	$\bar{3}$	0.0000	0.0000	0.0000
N[e]	$8c$	3	0.3378	0.3378	0.3378
O[e]	$24d$	1	0.2555	0.2837	0.4732
CaH_2[p]					
Ca	$4c$	m	0.2424	0.2500	0.1086
H	$4c$	m	0.3543	0.2500	0.4264
H	$4c$	m	−0.0273	0.2500	0.6775

[a] Values in these columns are in fractional unit cell units.

[b] Structure obtained from ref. 17. $P\bar{3}m1$; $a = b = 3.589$ Å; $c = 4.911$ Å; $\alpha = \beta = 90°$; $\gamma = 120°$; $V = 54.78$ Å^3; $Z = 1$.

[c] Structure obtained from the CSD, as reported by Burger *et al.*[18] CSD identity code: CAFORM02. *Pcab*; a = 10.168 Å; b = 13.407 Å; c = 6.278 Å; $\alpha = \beta = \gamma$ = 90°; V = 855.83 Å^3; Z = 8. We note here that the structure in the CSD does not agree fully with the reference account. In short, while the unit cell parameters are consistent with the experimental measurements reported at T = 296 K in the reference account, the atomic coordinates in CAFORM02 correspond to those measured at T = 100 K (from the same reference). We report calculations using the unit cell and atomic coordinates measured at T = 296 K.

[d] Structure obtained from the CSD, as reported by Matsui *et al.*[6] CSD identity code: CAFORM05. $P4_12_12$; $a = b$ = 6.776 Å; c = 9.453 Å; $\alpha = \beta = \gamma$ = 90°; V = 434.03 Å^3; Z = 4. Note: in the same literature account, a second structure under very similar measurement conditions was presented (CAFORM06). Relative to what we present above, we obtain very similar NMR tensor parameters using the H-optimized structure of CAFORM06 and hence we omit it from further discussion.

[e] Atomic positions have been optimized computationally, with computational details provided in Table S3.

[f] Structure obtained from ref. 7. *Pbcn*; a = 5.893 Å; b = 7.469 Å; c = 12.070 Å; $\alpha = \beta = \gamma$ = 90°; V = 531.26 Å^3; Z = 4.

[g] Structure obtained from the CSD, as reported by de Vries and Kroon.[8] CSD identity code: CIRZAE. $P2_1/c$; a = 8.921 Å; b = 10.300 Å; c = 9.881 Å; $\alpha = \gamma$ = 90°; β = 91.78°; V = 907.49 Å^3; Z = 4.

[h] Structure obtained from the CSD, as reported by Hawthorne *et al.*[9] CSD identity code: CATART01. $P2_12_12_1$; a = 9.631 Å; b = 10.573 Å; c = 9.215 Å; $\alpha = \beta = \gamma$ = 90°; V = 938.35 Å^3; Z = 4.

[i] Structure obtained from ref. 10. $P\bar{1}$; a = 6.241 Å; b = 8.214 Å; c = 10.411 Å; α = 94.92°; β = 106.00°; γ = 107.55°; V = 480.78 Å^3; Z = 2.

[j] Structure obtained from the CSD, as reported by Klop *et al.*[11] CSD identity code: CEJLIM. $P\bar{1}$; a = 6.750 Å; b = 11.076 Å; c = 11.782 Å; α = 116.49°; β = 92.40°; γ = 97.31°; V = 777.13 Å^3; Z = 4.

[k] Structure obtained from ref. 12. $P\bar{1}$; a = 6.700 Å; b = 9.801 Å; c = 12.257 Å; α = 78.83°; β = 86.21°; γ = 73.63°; V = 757.6 Å^3; Z = 4.

[l] Structure obtained from ref. 13. $C2/c$; a = 6.277 Å; b = 15.181 Å; c = 5.672 Å; $\alpha = \gamma$ = 90°; β = 114.11°; V = 493.34 Å^3; Z = 4.

[m] Structure obtained from the ICSD, as reported by Weber and Range.[19] ICSD identity code: 83387. $I4_1/amd$; $a = b$ = 7.222 Å; c = 6.285 Å; $\alpha = \beta = \gamma$ = 90°; V = 327.81 Å^3; Z = 4.

[n] Structure obtained from the ICSD, as reported by Ali and Yashima.[20] ICSD identity code: 153172. *Pbnm*; a = 5.3789 Å; b = 5.4361 Å; c = 7.6388 Å; $\alpha = \beta = \gamma$ = 90°; V = 223.36 Å^3; Z = 4.

[o] Structure obtained from the ICSD, as reported by Vegard and Bilberg.[14] ICSD identity code: 52351. $Pa\bar{3}$; $a = b = c$ = 7.615 Å; $\alpha = \beta = \gamma$ = 90°; V = 441.58 Å^3; Z = 4.

[p] Structure obtained from the ICSD, as reported by Alonso *et al.*[21] ICSD identity code: 260873. *Pnma*; a = 5.9600 Å; b = 3.6006 Å; c = 6.8167 Å; $\alpha = \beta = \gamma$ = 90°; V = 146.28 Å^3; Z = 4.

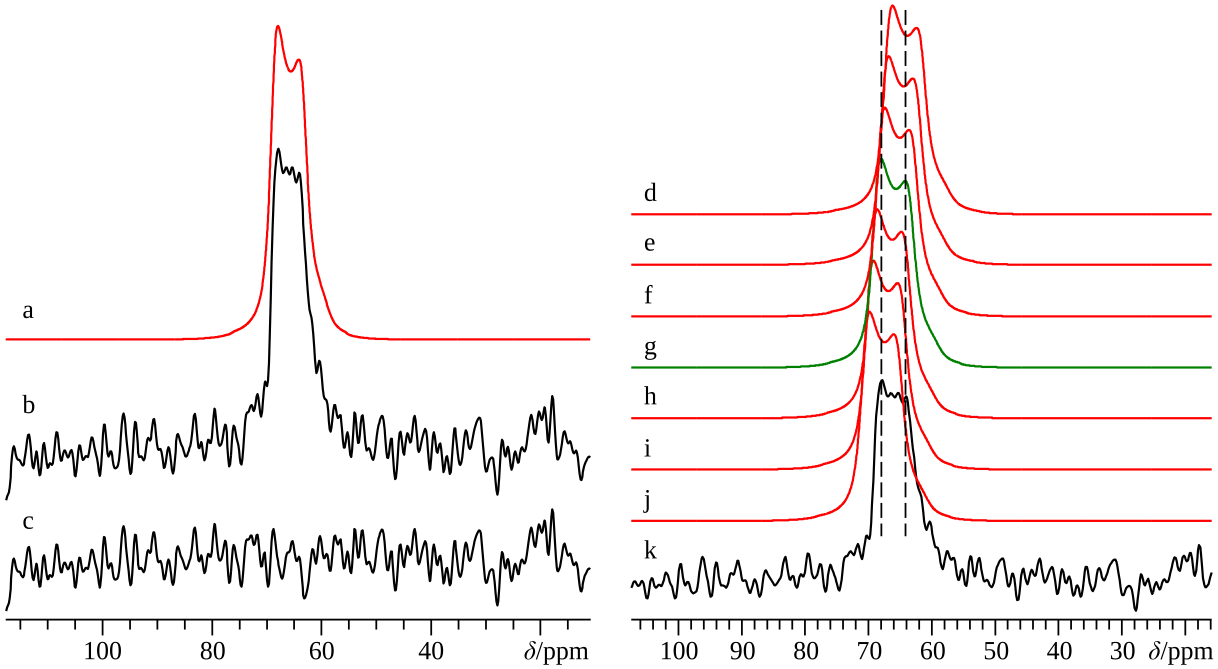

Figure S1. Analytical line shape simulations (a, d – j), and experimental Bloch decay ^{43}Ca MAS (ν_{MAS} = 5.00 kHz) SSNMR spectrum of Ca(OH)$_2$ acquired at B_0 = 21.1 T (b, k). The experimental spectrum is the result of the collection of 6 830 transients with a recycle delay of 10.0 s (experiment time = 19.0 h). In (c), the difference spectrum between (a) and (b) is presented. Analytical line shape simulations (d – j) illustrate the sensitivity of the line shape models to small changes in the calcium δ_{iso}. For these line shape simulations, all parameters are kept constant, except the value of δ_{iso}, which is varied as follows: (d) 68.6 ppm; (e) 69.2 ppm; (f) 69.8 ppm; (g) 70.4 ppm (best fit, same as (a)); (h) 71.0 ppm; (i) 71.6 ppm; (j) 72.2 ppm. The dashed lines are guides for the eye.

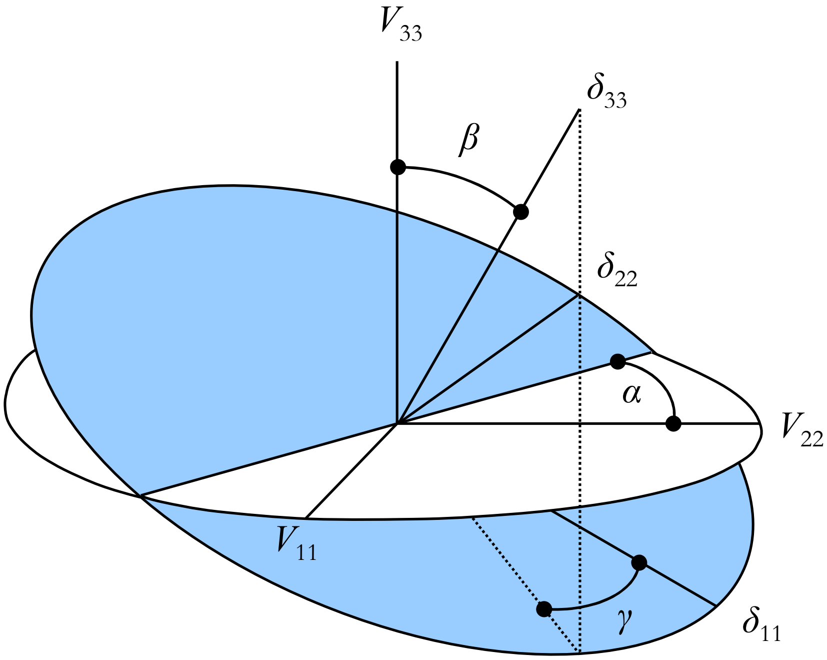

Figure S2. Schematic highlighting the relationship between the Euler angles (i.e., α, β, γ), and the relative orientation between the CS and EFG tensor PASs (illustration inspired by Eichele[24]). The angle of each counterclockwise rotation is determined by the value of each Euler angle and occurs in the order $\alpha \rightarrow \beta \rightarrow \gamma$. The convention used here assumes the EFG tensor PAS is static, while the CS tensor PAS is active. The eigenvectors shown (i.e., V_{11}, δ_{11}, etc.,) are associated with the tensor eigenvalues specified in Table S5.

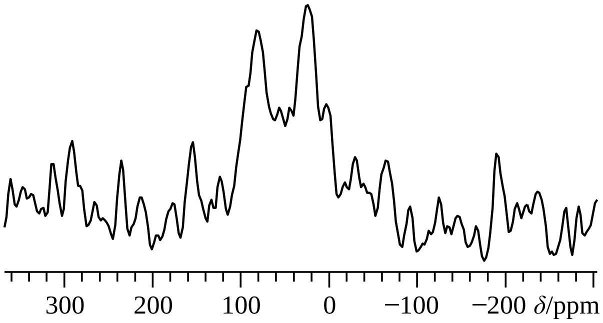

Figure S3. Experimental Bloch decay ^{43}Ca SSNMR spectrum of $Ca(OH)_2$ acquired at B_0 = 11.75 T under static conditions. The spectrum is the result of the collection of 63 228 transients with a recycle delay of 4.0 s (experiment time = 70.3 h). The calcium chemical shift scale is relative to a saturated solution of $CaCl_2$(*aq*).

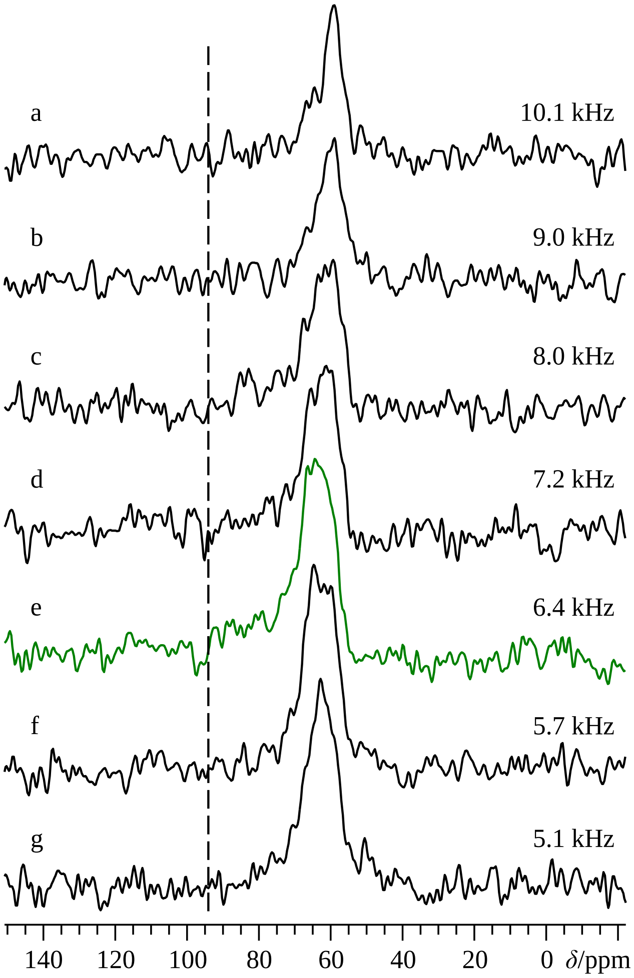

Figure S4. Experimental ^{43}Ca{^{1}H} CP/static SSNMR spectra of $Ca(OH)_2$, acquired at B_0 = 21.1 T, which illustrate the sensitivity of the experiment to variation in the radiofrequency field applied on the calcium channel during the cross-polarization contact period. All other relevant experimental parameters are kept constant and are as specified in Table S1. The radiofrequency field applied to the calcium channel is specified on the right portion of the figure. The dashed line is a guide to the eye and highlights additionally how certain crystallite orientations (manifested experimentally as signal at different resonance frequencies) are affected preferentially based upon the rf field applied to the calcium channel.

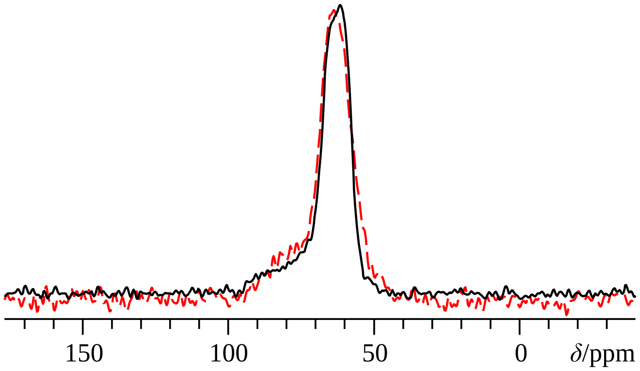

Figure S5. Experimental ^{43}Ca CP/static SSNMR spectra of Ca(OH)$_2$, acquired at B_0 = 21.1 T, which illustrate the effects of ^{1}H decoupling during the acquisition period. The black trace corresponds to the ^{1}H-decoupled spectrum (SPINAL64, $\nu_{rf}\{^1H\}$ = 19.2 kHz), while the red trace conserves all experimental parameters (please note the number of transients varies between the traces), except no ^{1}H decoupling field is applied during the ^{43}Ca signal acquisition period.

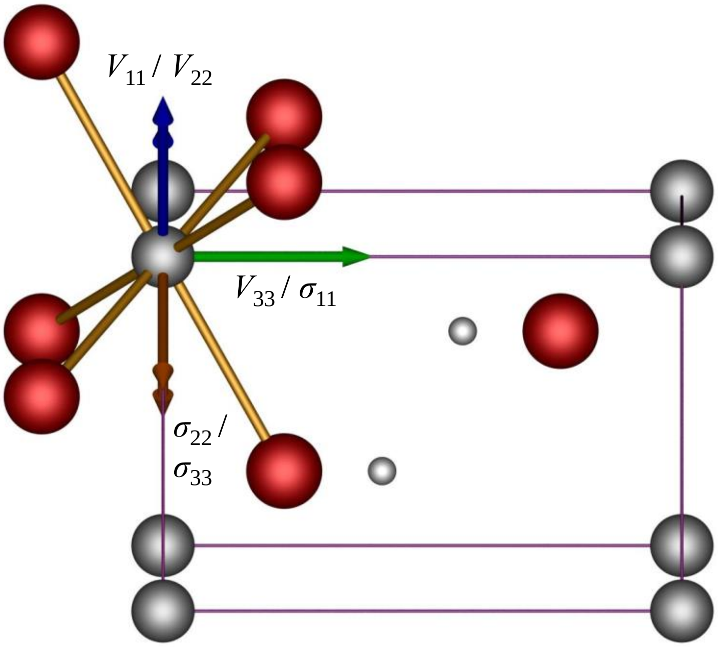

Figure S6. POV-Ray rendering of the computed calcium EFG tensor (V_{ii}, i = 1, 2, 3, in blue) and symmetric magnetic shielding (σ_{ii}, orange) tensor eigenvectors for Ca(OH)$_2$, highlighting both the unit cell and calcium first coordination sphere. Colour scheme remains as defined in the main paper. The eigenvectors are displayed once for each unique calcium, and were placed using Diamond v. 3.2i. When an EFG eigenvector overlaps with a shielding eigenvector, they are displayed in green. As $\eta_Q = 0$ and $\kappa = -1$, V_{11} and V_{22} are interchangeable, as are σ_{22} and σ_{33}; indeed, these eigenvectors span a plane of equivalent EFG, and equivalent magnetic shielding, respectively.

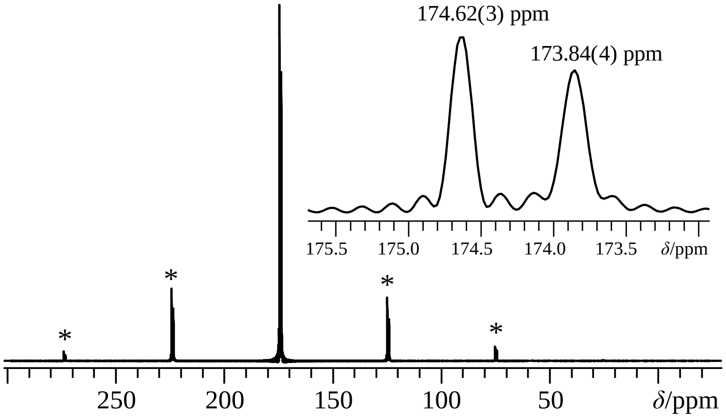

Figure S7. Experimental ^{13}C CP/MAS SSNMR spectrum of α-Ca(CHO$_2$)$_2$, acquired at B_0 = 9.4 T and ν_{MAS} = 5.0 kHz. Asterisks denote MAS spinning sidebands. Isotropic region has been expanded and inset, and measured chemical shifts are indicated.

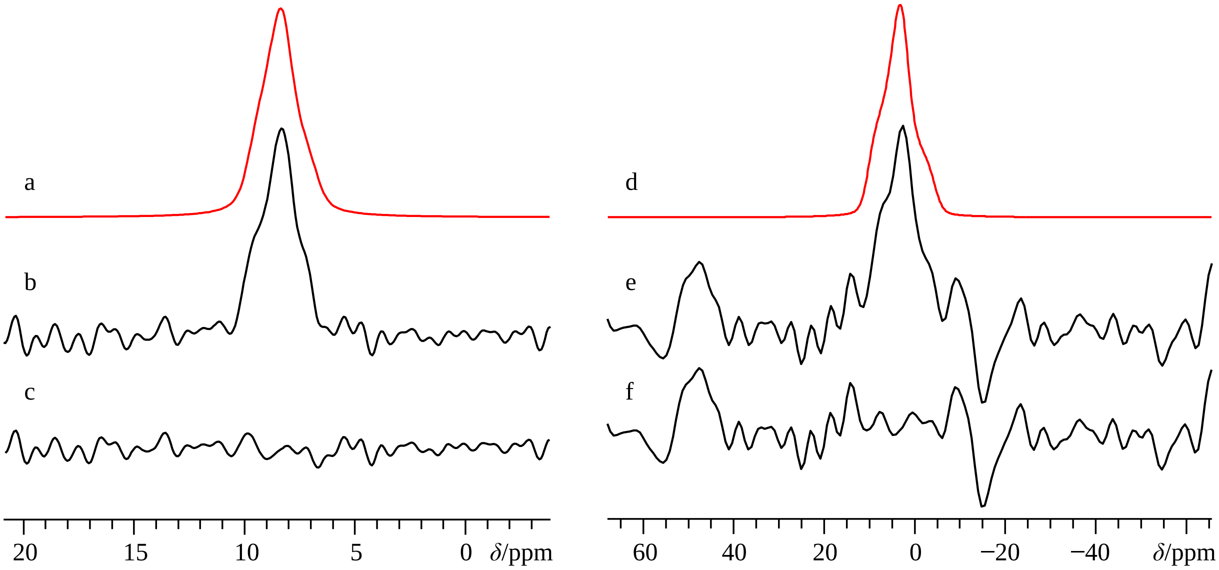

Figure S8. Analytical line shape simulations (a, d), and experimental Bloch decay ^{43}Ca MAS (ν_{MAS} = 5.00 kHz) SSNMR spectra of α-Ca(CHO$_2$)$_2$ acquired at B_0 = 21.1 T (b), and B_0 = 9.4 T (e). The experimental spectra result from the collection of 4 096 transients with a recycle delay of 5.0 s in (b), and from the collection of 21 144 transients with a recycle delay of 10.0 s in (e), which infers experiment times of 5.7 h and 58.7 h, respectively. In (c) and (f), the appropriate difference spectra between the experimental and simulation spectra are provided.

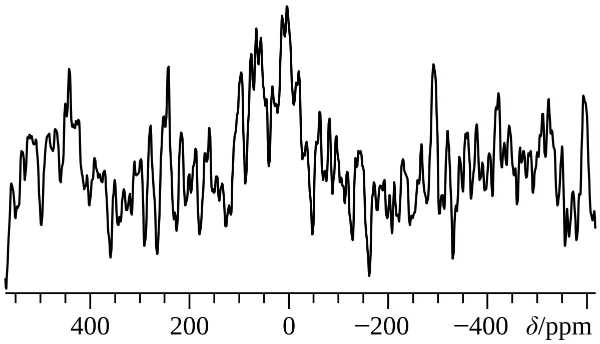

Figure S9. Experimental Bloch decay ^{43}Ca SSNMR spectrum of $CaCl_2·2H_2O$ acquired at B_0 = 11.75 T under static conditions. The spectrum is the result of the collection of 47 787 transients with a recycle delay of 5.0 s (experiment time = 66.4 h). The calcium chemical shift scale is relative to a saturated solution of $CaCl_2$(*aq*).

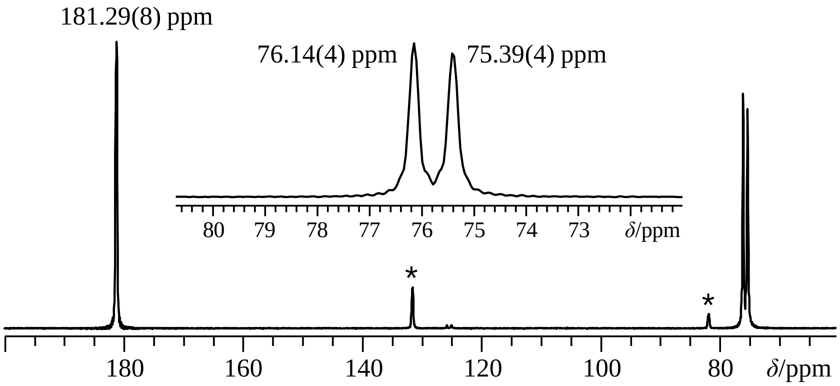

Figure S10. Experimental ^{13}C CP/MAS SSNMR spectrum of (±)-$Ca(C_4H_4O_6)·4H_2O$, acquired at B_0 = 9.4 T and ν_{MAS} = 5.0 kHz. Asterisks denote MAS spinning sidebands. Isotropic region has been expanded and inset, and measured chemical shifts are indicated. All observed ^{13}C chemical shifts for this sample are distinct from DL-tartaric acid.

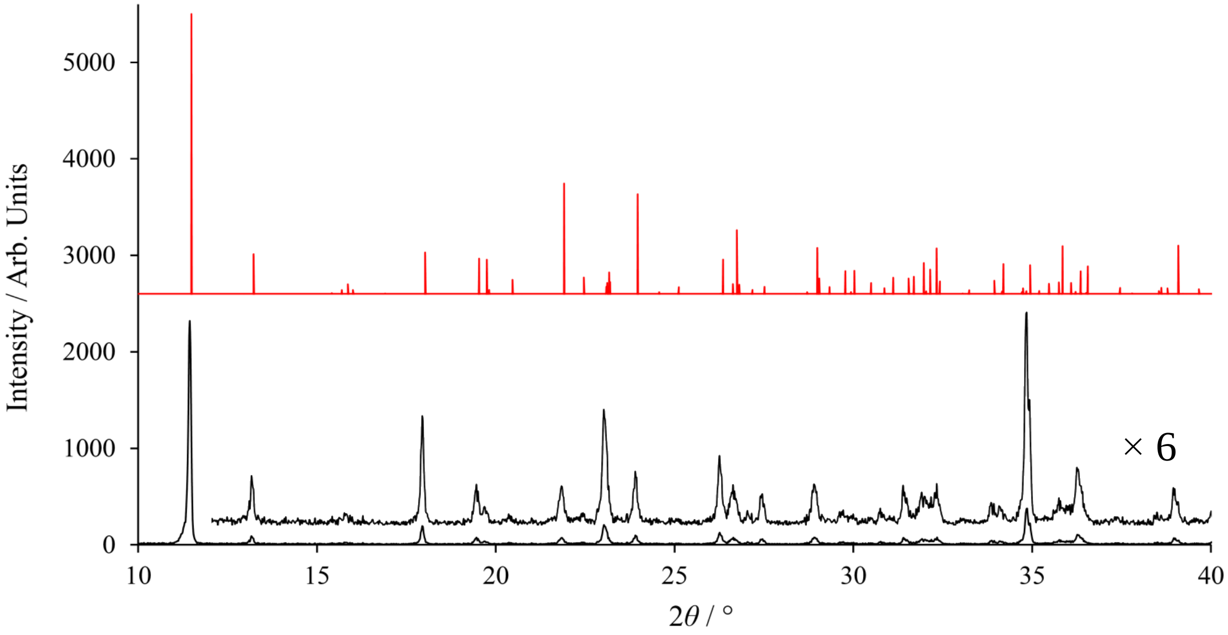

Figure S11. Experimental powder XRD results of (±)-Ca($C_4H_4O_6$)·4H_2O (bottom trace), along with the simulated diffraction pattern which is expected to result based upon the published structure of Le Bail *et al.*[10] The agreement is substantially better relative to the case where the other known form[9,25,26] of (+)-Ca($C_4H_4O_6$)·4H_2O is assumed.

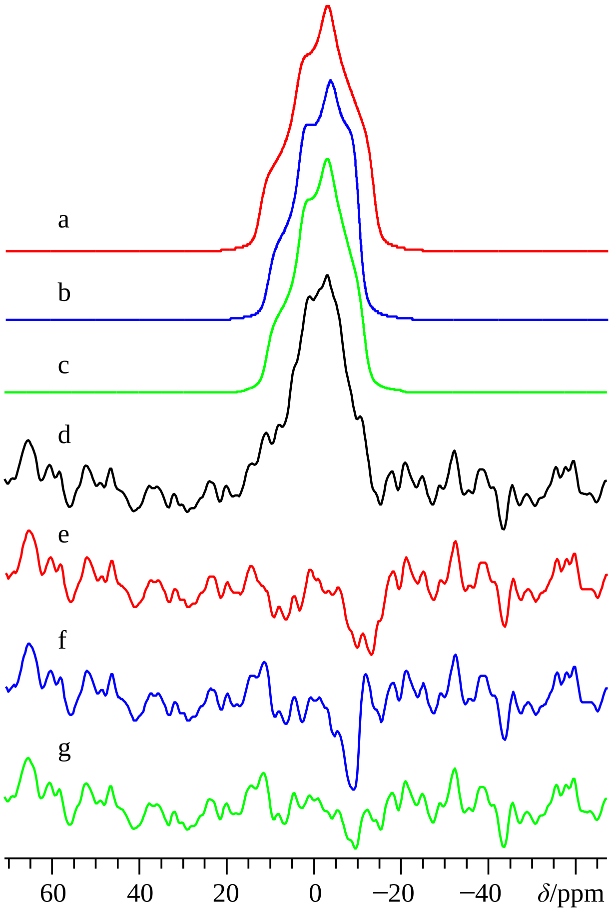

Figure S12. Analytical line shape simulations (a – c) and experimental ^{43}Ca SSNMR spectrum (d) of (±)-$Ca(C_4H_4O_6)\cdot 4H_2O$ under static conditions at B_0 = 21.1 T. The difference spectra in (e), (f), and (g) are generated by taking the difference between (a) and (d), (b) and (d), and (c) and (d), respectively, and are meant to highlight the goodness of the extracted ^{43}Ca NMR tensor parameters. The simulated spectrum in (c) corresponds to the best fit to the experimental data, and uses the parameters reported in Table 2 of the main text. Simulated spectra in (a) and (b) retain the same parameters as in (c), except that in (a) Ω = 27 ppm and in (b) β = 90°, and which were chosen as these values lie just outside the reported error region.

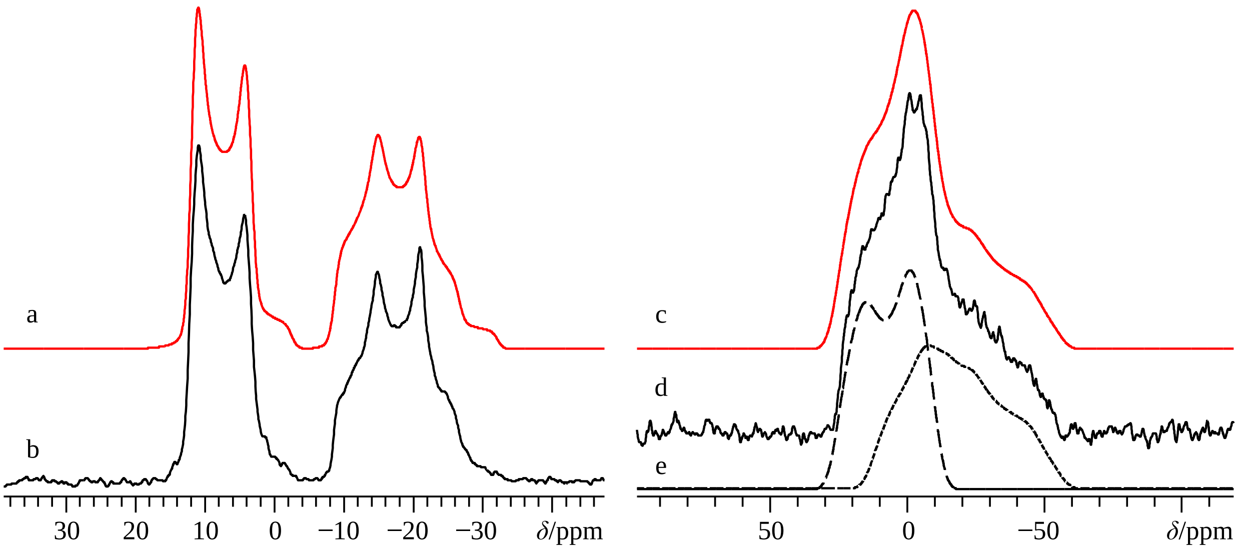

Figure S13. Analytical line shape simulations (a, c, e), experimental FSG-RAPT ^{43}Ca MAS SSNMR spectrum (b) under ν_{MAS} = 5.0 kHz, and experimental Hahn echo ^{43}Ca{^{1}H} static SSNMR spectrum (d) at B_0 = 9.4 T of enriched (ca. 7 %) ^{43}Ca($C_2H_3O_2$)$_2$·H_2O. The experimental spectrum in (b) results from the collection of 768 transients with a recycle delay of 9.0 s for an experimental time of 1.9 hours, while that in (d) is from 4 096 transients with a recycle delay of 9.0 s (10.2 h). A deconvolution of the two sites is provided in (e).

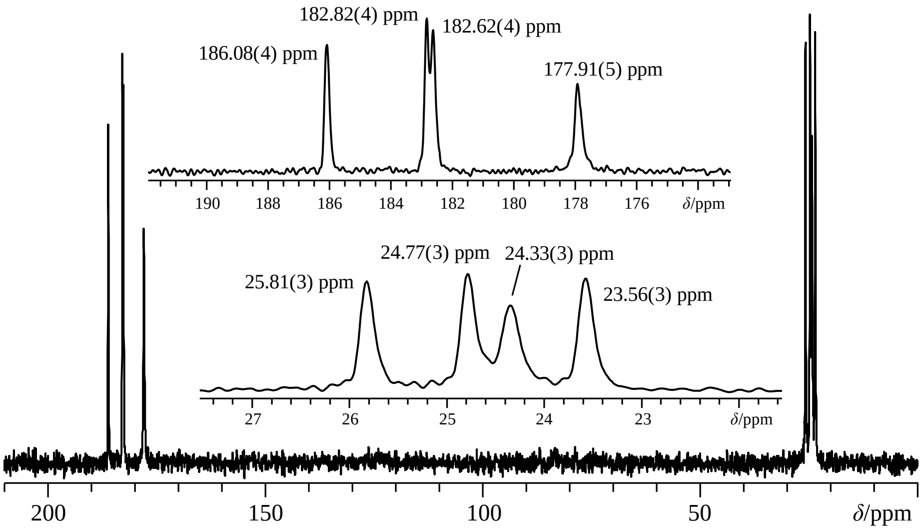

Figure S14. Experimental ^{13}C CP/MAS SSNMR spectrum of Ca($C_2H_3O_2$)$_2$·H_2O, acquired at B_0 = 4.7 T and ν_{MAS} = 5.0 kHz. Isotropic regions have been expanded, inset, and measured chemical shifts are indicated.

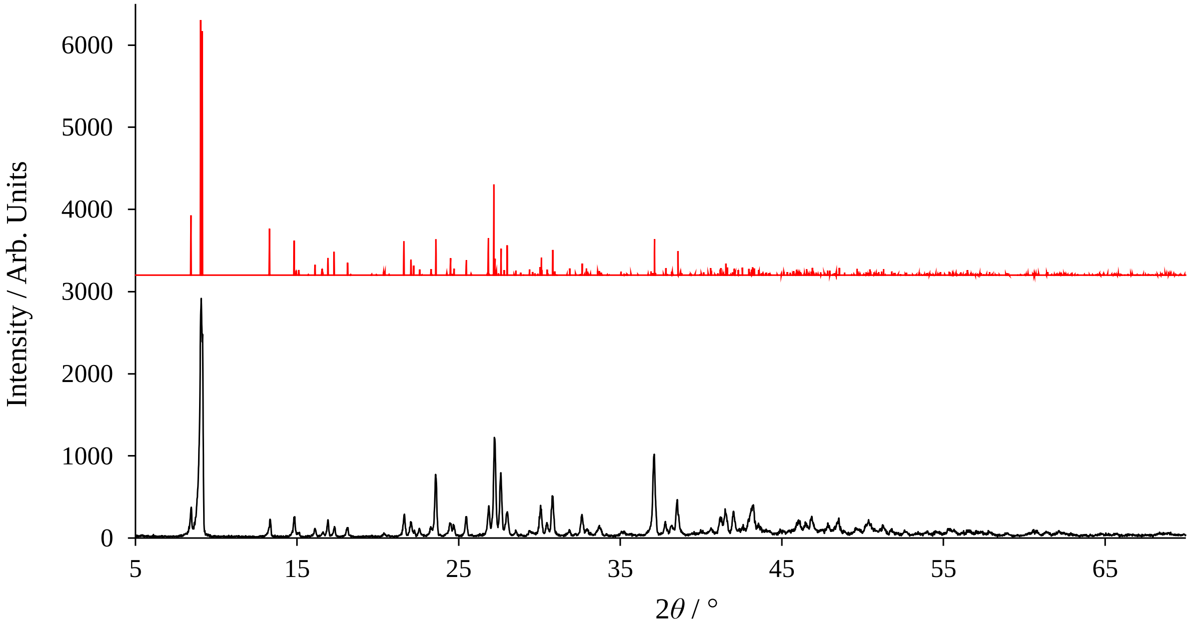

Figure S15. Experimental powder XRD results of $Ca(C_2H_3O_2)_2{\cdot}H_2O$ (bottom trace), along with the simulated diffraction pattern which is expected to result based upon the published structure of Klop *et al.*[11] The present agreement is much better relative to the case where the other known polymorphic form[12] of $Ca(C_2H_3O_2)_2{\cdot}H_2O$ is used.

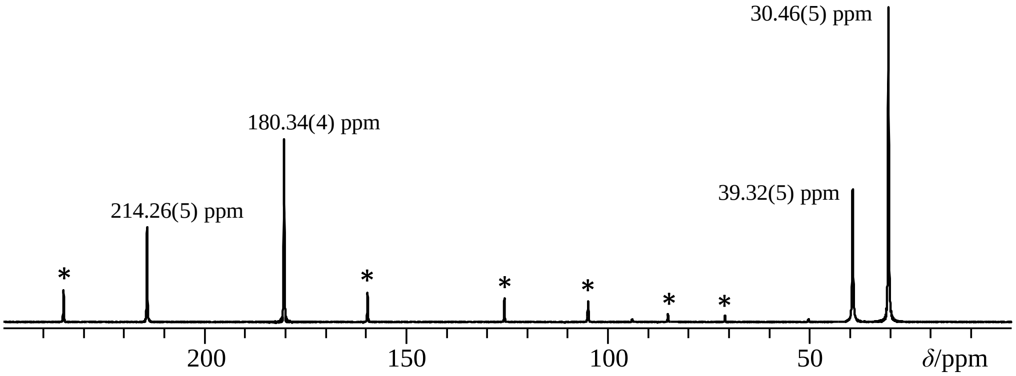

Figure S16. Experimental ^{13}C CP/MAS SSNMR spectrum of $Ca(C_5H_7O_3)_2{\cdot}2H_2O$, acquired at B_0 = 9.4 T and ν_{MAS} = 5.5 kHz. Asterisks denote spinning sidebands.

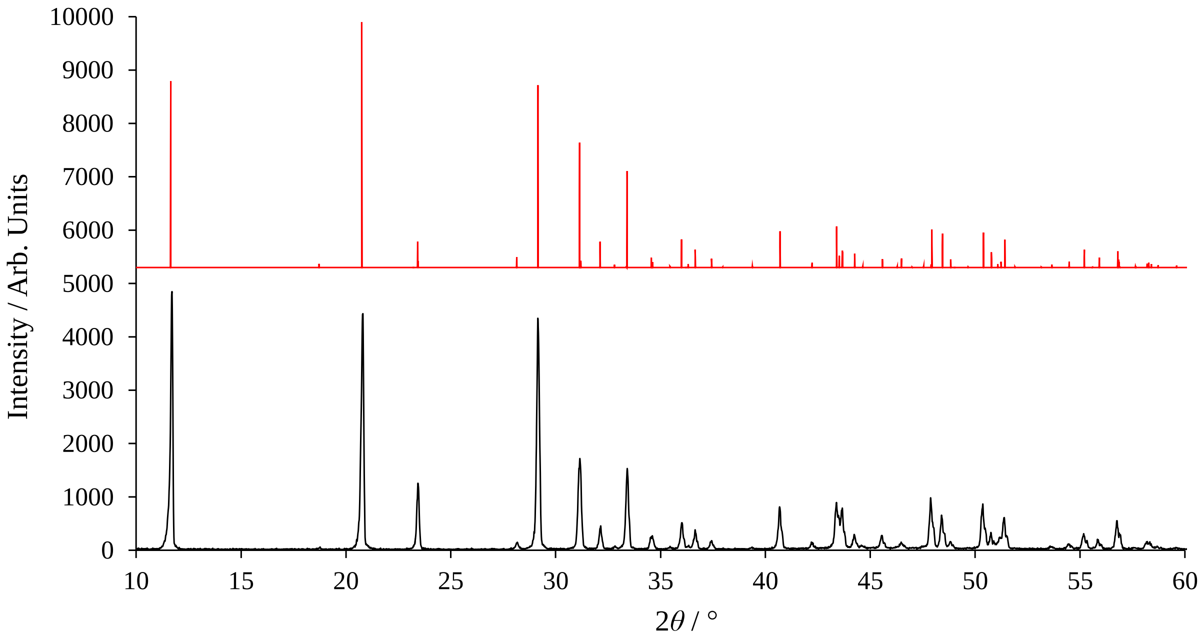

Figure S17. Experimental powder XRD results of $CaSO_4 \cdot 2H_2O$ (bottom trace), along with the simulated diffraction pattern which is expected to result based upon the published structure of Comodi *et al.*[13] The present agreement is much better relative to the case where the other suggested structures of $CaSO_4 \cdot 2H_2O$ are used,[27] notably, the experimental absence of a very strong diffraction peak near $2\theta = 16.5°$, which is found in the calculated diffraction patterns using these other suggested crystal structures.

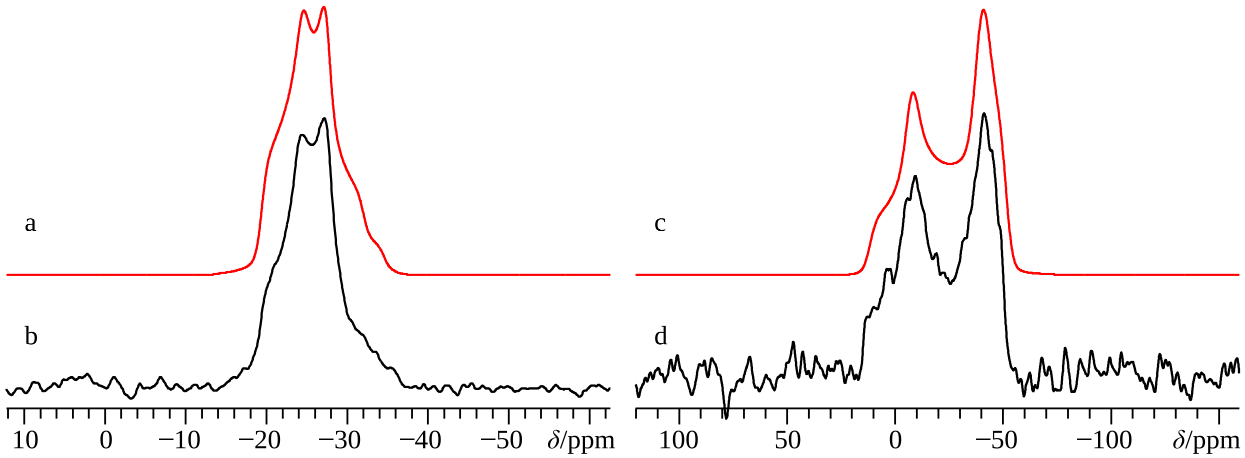

Figure S18. Analytical line shape simulations (a, c), experimental DFS/echo ^{43}Ca MAS (ν_{MAS} = 5.00 kHz, b), and experimental Hahn echo ^{43}Ca{^{1}H} static (d) SSNMR spectra of enriched $^{43}Ca^{33}SO_4 \cdot 2H_2O$ (ca. 7 % ^{43}Ca), acquired at B_0 = 9.4 T. The experimental spectra result from the collection of 32 transients with a recycle delay of 250 s in (b) (experimental time = 2.2 h), and from the collection of 336 transients with a recycle delay of 180 s in (d) (experimental time = 16.8 h).

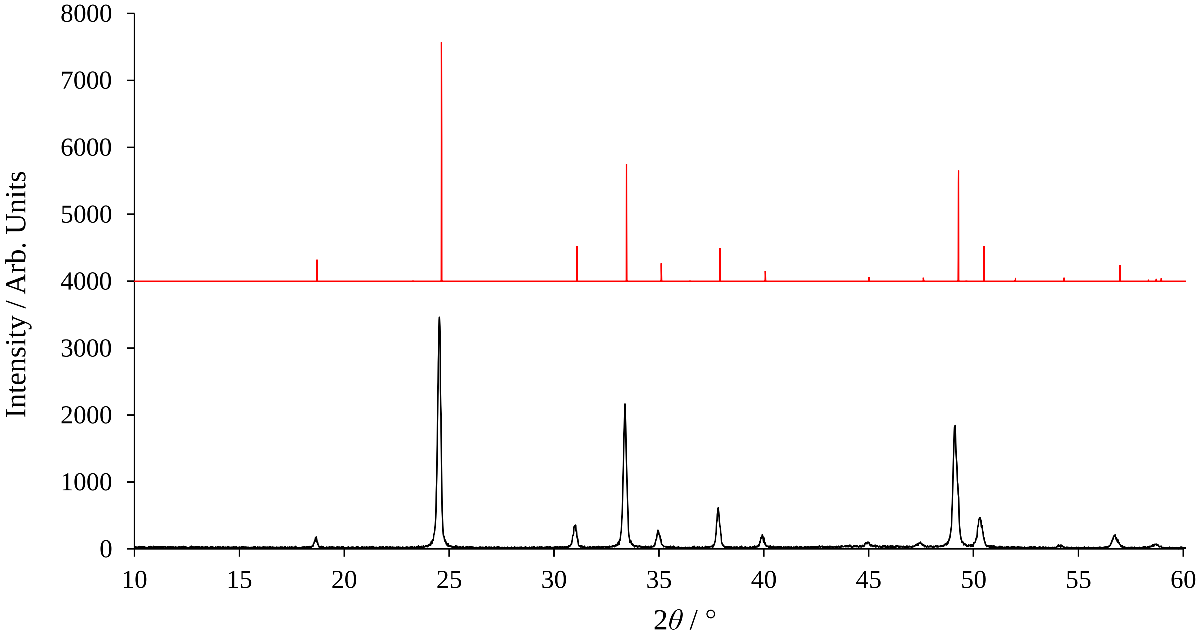

Figure S19. Experimental powder XRD results of $CaCrO_4$ (bottom trace), along with the simulated diffraction pattern which is expected to result based upon the published structure of Weber and Range.[19]

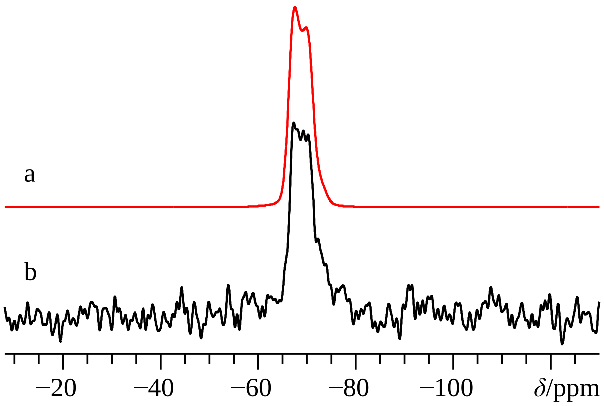

Figure S20. Analytical line shape simulation (a), and experimental Bloch decay ^{43}Ca MAS (ν_{MAS} = 4.00 kHz, b) SSNMR spectrum of $CaCrO_4$ acquired at B_0 = 9.4 T. The experimental spectrum results from the collection of 65 536 transients with a recycle delay of 2.0 s (experimental time = 36.4 h).

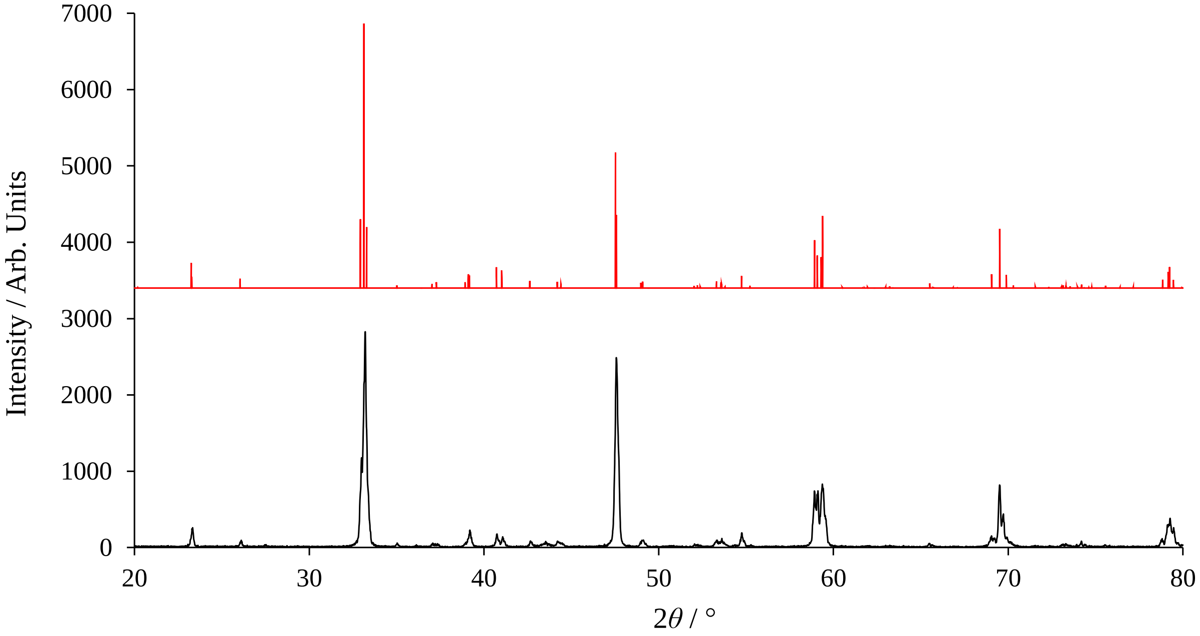

Figure S21. Experimental powder XRD results of $CaTiO_3$ (bottom trace), along with the simulated diffraction pattern which is expected to result based upon the published structure of Ali and Yahshima.[20]

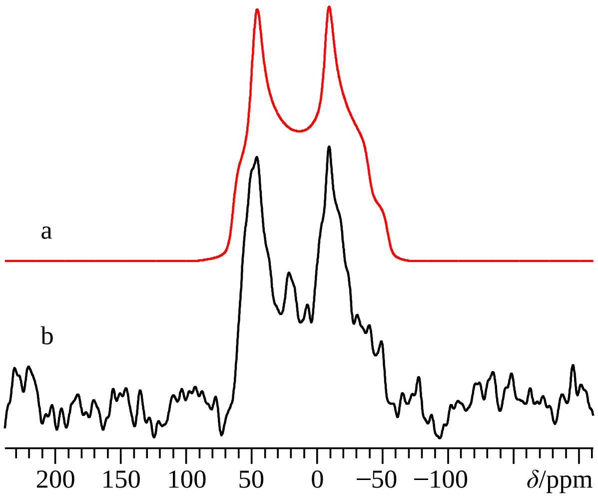

Figure S22. Analytical line shape simulation (a), and experimental Hahn echo ^{43}Ca static SSNMR spectrum (b) of $CaTiO_3$ acquired at B_0 = 11.75 T. The experimental spectrum results from the collection of 34 816 transients with a recycle delay of 5.0 s (experimental time = 48.4 h).

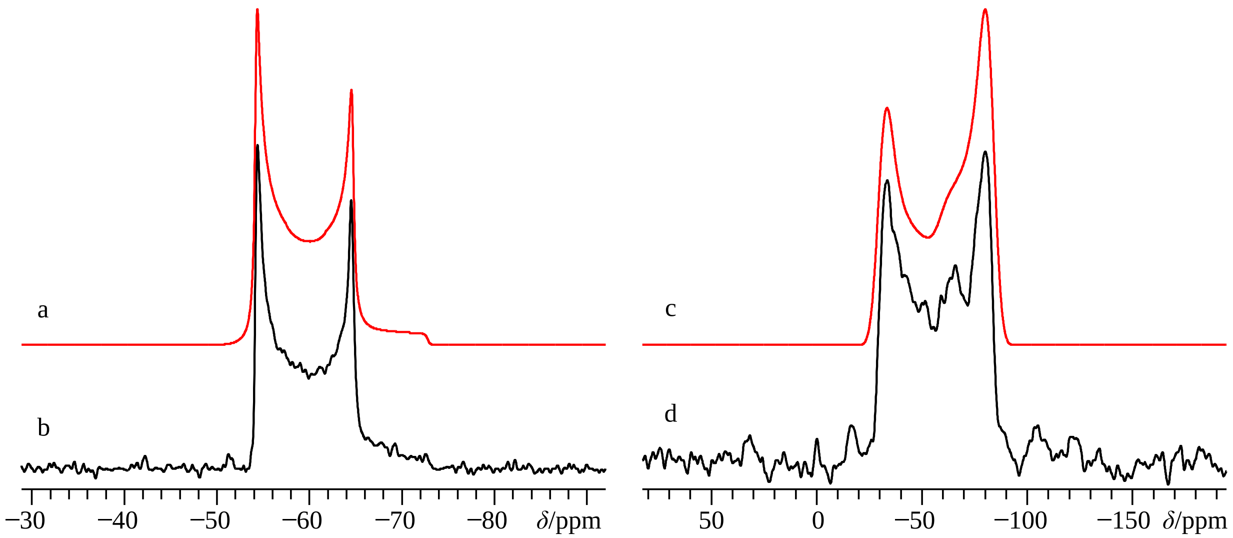

Figure S23. Analytical line shape simulations (a, c), experimental DFS/echo ^{43}Ca MAS (ν_{MAS} = 5.00 kHz, b), and experimental Hahn echo ^{43}Ca static (d) SSNMR spectra of enriched ^{43}Ca(NO$_3$)$_2$ (ca. 7% ^{43}Ca) acquired at B_0 = 9.4 T. The experimental spectra result from the collection of 64 transients with a recycle delay of 15 s in (b), and from the collection of 192 transients with a recycle delay of 15 s in (d) for experimental times of 16 and 48 minutes, respectively.

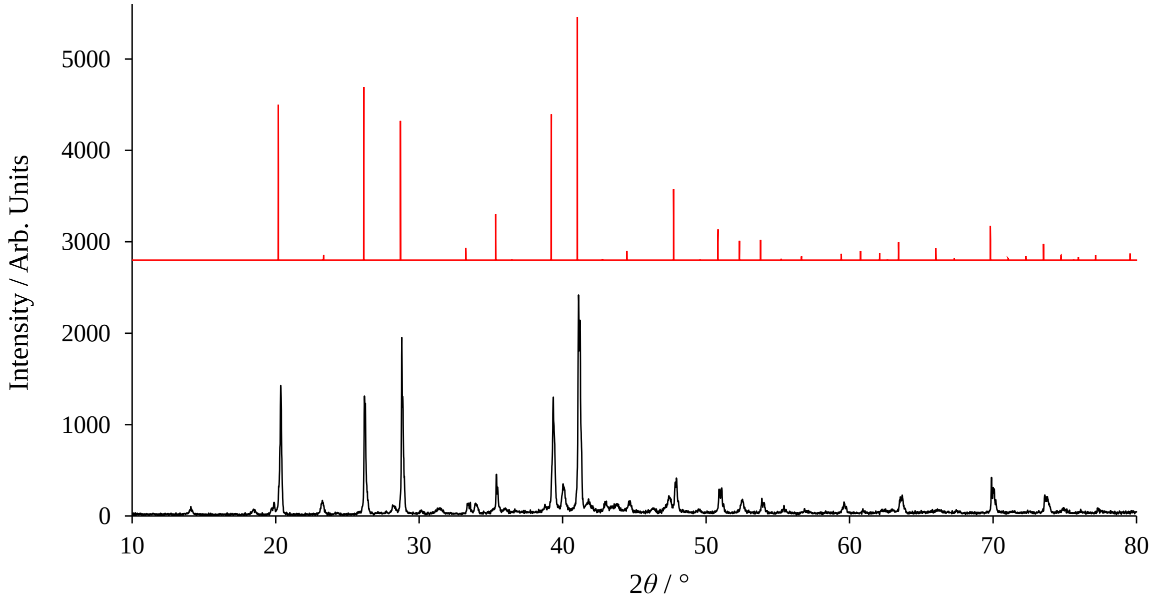

Figure S24. Experimental powder XRD results of Ca(NO$_3$)$_2$ (bottom trace), along with the simulated diffraction pattern which is expected to result based upon the published structure of Vegard and Bilberg.[14] The structure obtained after GIPAW DFT optimization of the N and O atoms did not lead to a significantly altered pXRD diffractogram relative to the one displayed above.

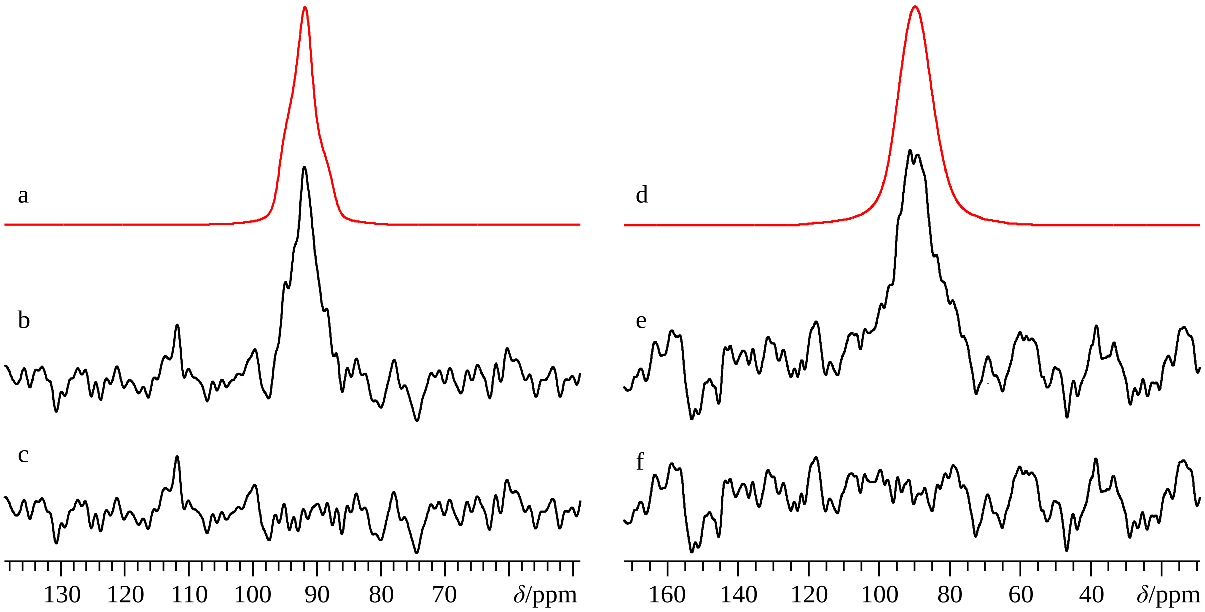

Figure S25. Analytical line shape simulations (a, d), experimental Bloch decay $^{43}Ca\{^1H\}$ MAS SSNMR spectrum under ν_{MAS} = 6.0 kHz and B_0 = 11.75 T (b), and ^{43}Ca MAS SSNMR spectrum under ν_{MAS} = 2.5 kHz and B_0 = 9.4 T (d) of CaH_2, as well as corresponding difference spectra in (c) and (f). The experimental spectra result from the collection of 8 192 transients with a recycle delay of 60 s in (b), and from the collection of 24 576 transients with a recycle delay of 10 s in (d) for experimental times of 136.5 hours and 68.3 hours, respectively.

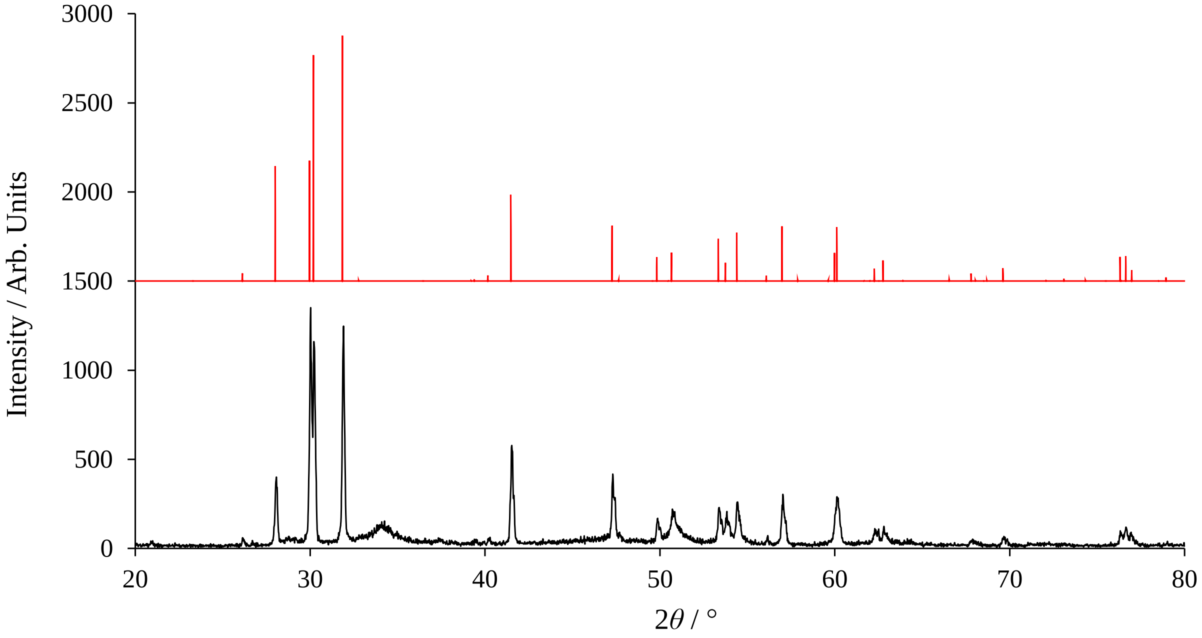

Figure S26. Experimental powder XRD results of CaH_2 (bottom trace), along with the simulated diffraction pattern which is expected to result based upon the published structure of Alonso *et al.*[21] A minor (disordered) component is clearly visible (2θ = ca. 33°), but its presence clearly does not impact the NMR results discussed herein.

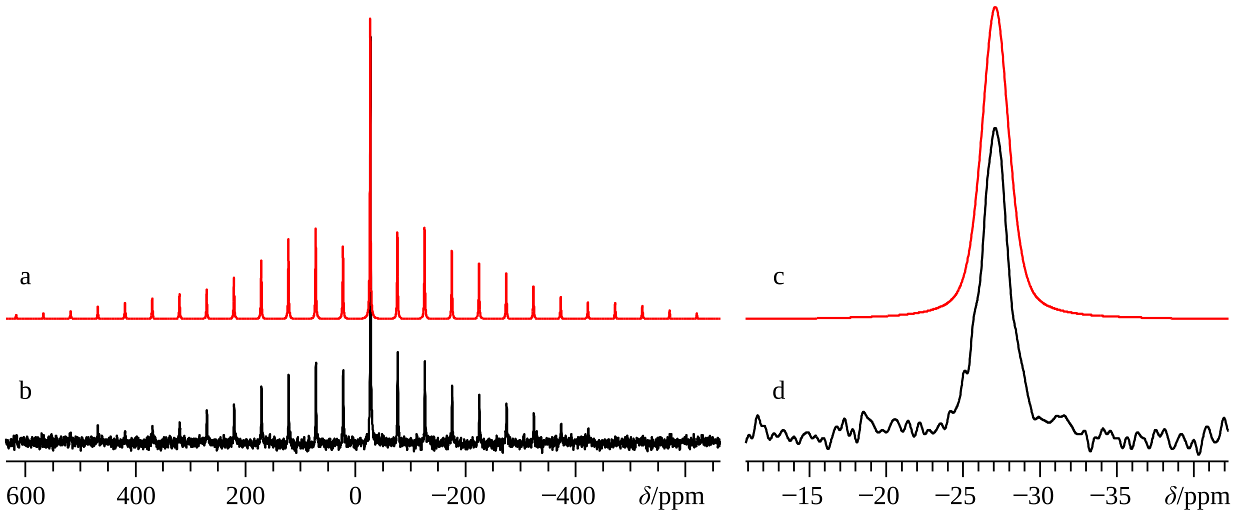

Figure S27. Numerical line shape simulation (a), analytical line shape simulation (c), and experimental Bloch decay ^{43}Ca MAS SSNMR spectra under ν_{MAS} = 3.0 kHz and B_0 = 21.1 T (b), and under ν_{MAS} = 5.0 kHz and B_0 = 11.75 T (d) of a natural sample of $CaCO_3$ (aragonite polymorph from clam pearl in (b), and from coral in (d)). The experimental spectra result from the collection of 16 384 transients with a recycle delay of 2.1 s in (b), and from the collection of 65 440 transients with a recycle delay of 2.0 s in (d) for experimental times of 9.6 hours and 36.4 hours, respectively.

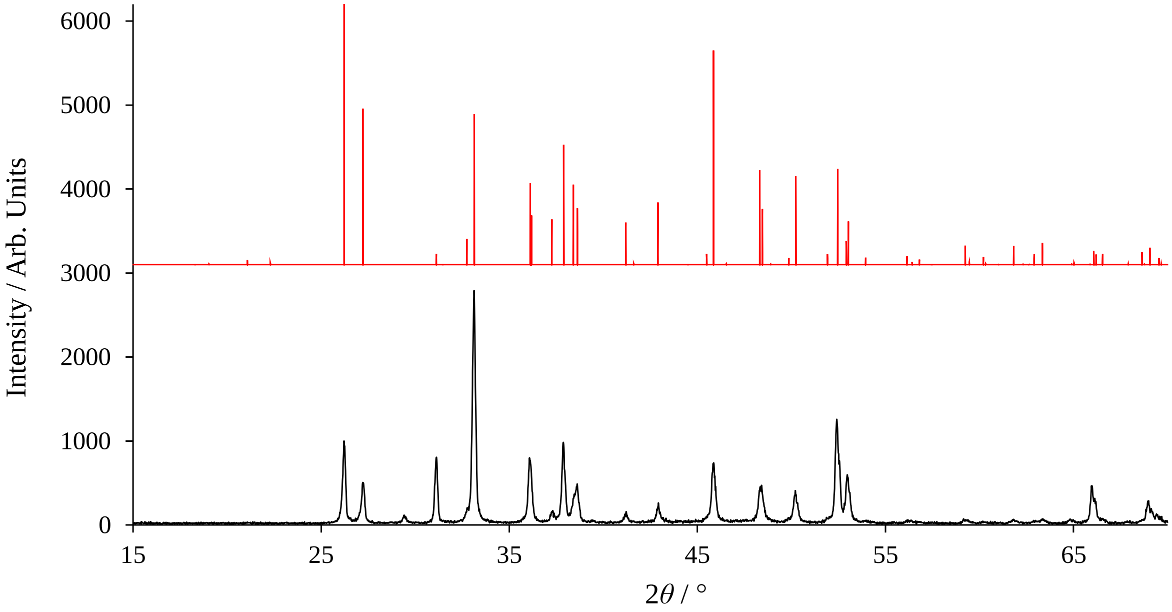

Figure S28. Experimental powder XRD results of natural $CaCO_3$ (aragonite polymorph), along with the simulated diffraction pattern which is expected to result based upon the published structure of Caspi *et al.*[28] No evidence of the calcite (or any other known) polymorph of $CaCO_3$ is observed.

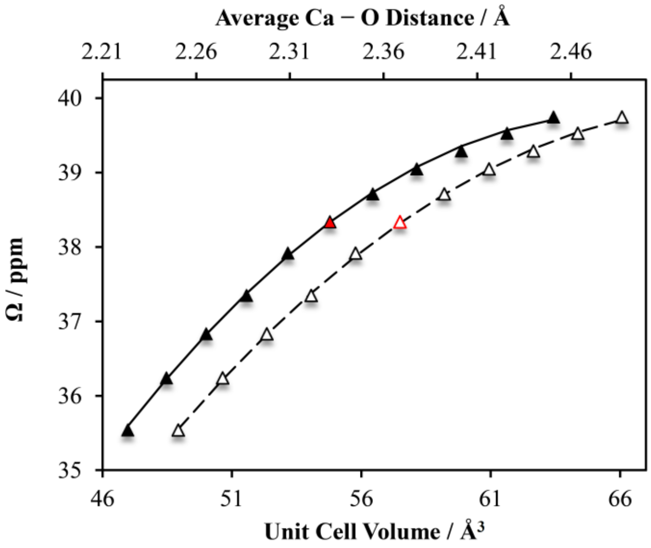

Figure S29. Results of GIPAW DFT computations which highlight the subtle changes in the calcium shift tensor span value (Ω) to minor alterations in the structural parameters of $Ca(OH)_2$. The data points indicated in red correspond to the Ω calculated using the accepted crystal structure. Solid data points correspond to lower horizontal axis. Second-degree polynomial line of best fit: $\Omega = -0.1168(V_{\text{cell}})^2 + 1.540(V_{\text{cell}}) - 10.97$, $R^2 = 0.999$, where V_{cell} is the unit cell volume in Å^3. Open data points correspond to upper horizontal axis. Second-degree polynomial fit: $\Omega = -49.28(r_{\text{Ca-O}})^2 + 251.0(r_{\text{Ca-O}}) - 279.8$; $R^2 = 1.00$, where $r_{\text{Ca-O}}$ is the average calcium-oxygen distance in Å.

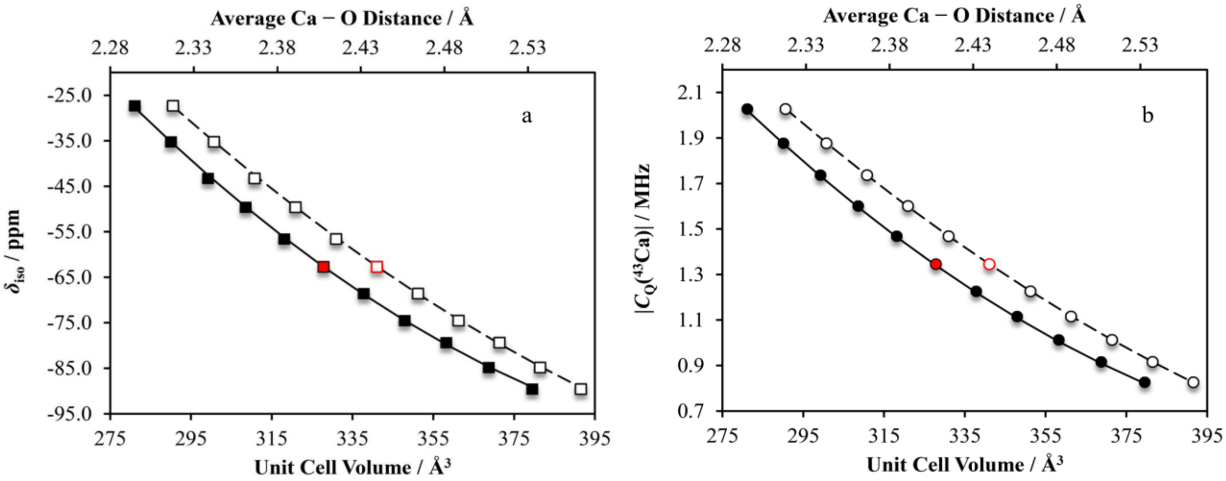

Figure S30. Results of GIPAW DFT computations which highlight the sensitivity of the isotropic calcium chemical shift (a), and the $|C_Q(^{43}Ca)|$ value (b) to minor alterations in the structural parameters of $CaCrO_4$. Unit cell volumes were changed in an isotropic fashion (i.e., uniform expansion or contraction). The data points indicated in red correspond to the respective parameters calculated using the accepted crystal structure. Solid data points correspond to lower horizontal axis. Second-degree polynomial lines of best fit: in a, $\delta_{\text{iso}} = 0.002395(V_{\text{cell}})^2 - 2.206(V_{\text{cell}}) + 403.2$, $R^2 = 0.997$; in b, $|C_Q(^{43}Ca)| = 4.610 \times 10^{-5}(V_{\text{cell}})^2 - 0.04264(V_{\text{cell}}) + 10.36$, $R^2 = 1.00$. Open data points correspond to upper horizontal axis. Second-degree polynomial fit: in a, $\delta_{\text{iso}} = 288.0(r_{\text{Ca-O}})^2 - 1658(r_{\text{Ca-O}}) + 2269$, $R^2 = 1.00$; in b, $|C_Q(^{43}Ca)| = 5.487(r_{\text{Ca-O}})^2 - 31.70(r_{\text{Ca-O}}) + 46.03$, $R^2 = 1.00$.

References

1 S. Hayashi and K. Hayamizu, *Bull. Chem. Soc. Jpn.*, 1991, **64**, 685-687.

2 M. Bak, J. T. Rasmussen and N. C. Nielsen, *J. Magn. Reson.*, 2000, **147**, 296-330.

3 A. E. Bennett, C. M. Rienstra, M. Auger, K. V. Lakshmi and R. G. Griffin, *J. Chem. Phys.*, 1995, **103**, 6951-6958.

4 B. M. Fung, A. K. Khitrin and K. Ermolaev, *J. Magn. Reson.*, 2000, **142**, 97-101.

5 S. Prasad, H.-T. Kwak, T. Clark and P. J. Grandinetti, *J. Am. Chem. Soc.*, 2002, **124**, 4964-4965.

6 M. Matsui, T. Watanabe, N. Kamijo, R. L. Lapp and R. A. Jacobson, *Acta Cryst. B,* 1980, **B36**, 1081-1086.

7 A. Leclaire and M. M. Borel, *Acta. Cryst. B,* 1977, **B33**, 1608-1610.

8 A. J. de Vries and J. Kroon, *Acta Cryst. C,* 1984, **C40**, 1542-1544.

9 F. C. Hawthorne, I. Borys and R. B. Ferguson, *Acta. Cryst. B,* 1982, **B38**, 2461-2463.

10 A. Le Bail, D. Bazin, M. Daudon, A. Brochot, V. Robbez-Masson and V. Maisonneuve, *Acta Cryst. B,* 2009, **B65**, 350-354.

11 E. A. Klop, A. Schouten, P. van der Sluis and A. L. Spek, *Acta Cryst. C,* 1984, **C40**, 51-53.

12 P. van der Sluis, A. Schouten and A. L. Spek, *Acta Cryst. C,* 1987, **C43**, 1922-1924.

13 P. Comodi, S. Nazzareni, P. F. Zanazzi and S. Speziale, *Am. Mineral.*, 2008, **93**, 1530-1537.

14 L. Vegard and L. Bilberg, *Skrifter utgitt av det Norske videnskaps-Akademi i Oslo 1: Matematisk-Naturvidenskapelig Klasse*, 1931, **12**, 1-22.

15 J. P. Perdew, K. Burke and M. Ernzerhof, *Phys. Rev. Lett.*, 1996, **77**, 3865-3868.

16 J. P. Perdew, K. Burke and M. Ernzerhof, *Phys. Rev. Lett.*, 1997, **78**, 1396.

17 L. Desgranges, D. Grebille, G. Calvarin, G. Chevrier, N. Floquet and J.-C. Niepce, *Acta Cryst. B,* 1993, **B49**, 812-817.

18 N. Burger, H. Fuess and S. A. Mason, *Acta. Cryst. B,* 1977, **B33**, 1968-1970.

19 G. Weber and K. J. Range, *Z. Naturforsch. B,* 1996, **51**, 751-753.

20 R. Ali and M. Yashima, *J. Solid State Chem.*, 2005, **178**, 2867-2872.

21 J. A. Alonso, M. Retuerto, J. Sánchez-Benítez and M. T. Fernández-Díaz, *Z. Kristallogr.*, 2010, **225**, 225-229.

22 B. K. Sahoo, *Phys. Rev. A,* 2009, **80**, 012515.

23 I. L. Moudrakovski, R. Alizadeh and J. J. Beaudoin, *Phys. Chem. Chem. Phys.*, 2010, **12**, 6961-6969.

24 K. Eichele and R. E. Wasylishen, WSolids1, version 1.19.11, Universität Tübingen, Tübingen, Germany, 2009.

25 G. K. Ambady, *Acta. Cryst. B*, 1968, **B24**, 1548-1557.

26 R. Boese and O. Heinemann, *Z. Kristallogr.*, 1993, **205**, 348-349.

27 B. F. Pedersen and D. Semmingsen, *Acta Cryst. B,* 1982, **B38**, 1074-1077.

28 E. N. Caspi, B. Pokroy, P. L. Lee, J. P. Quintana and E. Zolotoyabko, *Acta Cryst. B,* 2005, **B61**, 129-132.